MODELING THE PERFORMANCE OF SPIRAL-WOUND MEMBRANES IN A PRESSURE-RETARDED OSMOSIS PROCESS

A Thesis

by

SALY MONIR MATTA

Submitted to the Office of Graduate and Professional Studies of
Texas A&M University
in partial fulfillment of the requirements for the degree of

MASTER OF SCIENCE

Chair of Committee,	Ahmed Abdel-Wahab
Co-Chair of Committee,	Marcelo Castier
Committee Members,	Eyad Masad
Head of Department,	Patrick Linke

May 2021

Major Subject: Chemical Engineering

ABSTRACT

A process simulator has been developed to model and predict the performance of spiral-wound membrane modules in a pressure retarded osmosis process. This has involved automation of generalized protocols for the numerical integration of the solvent and solute flux equations, in conjunction with a suitable electrolyte equation of state, along the surface area of a spiral-wound membrane leaf. Performance equations are solved for discrete area elements and the spiral-wound character of the module as a whole is realized through the programmed sequence in which discrete elements are evaluated. This arrangement allows for mirroring the parabolic flow pattern of the feed stream in the spiral-wound membrane leaf. The total permeation and, by extension, power density, is thus calculated in a manner that accounts for the driving force profile consistent with flow patterns specific to spiral-wound membranes. This effective treatment of each discrete element as a flat-sheet membrane enables the transferability of membrane parameters characterized in standard, coupon-scale experiments to the simulation of spiral-wound modules. This transferability is illustrated through comparisons of model predictions with published pilot-scale PRO data.

ACKNOWLEDGEMENTS

I would like to truly thank Dr Ahmed Abdel-Wahab and Dr. Castier for their tremendous support and guidance throughout my research journey. Their valuable input and constructive feedback allowed me to successfully complete my research project. My gratitude also extends to Dr. Masad, who was available to offer valuable input to any questions/doubts I had.

I am beyond thankful to Muaz Selam and Husnain Manzoor for dedicating a lot of time and effort to help me enhance my FORTRAN programming skills. Their expertise and mentorship have helped me complete the project tasks in a timely and efficient manner.

Last but certainly not least, I am grateful to my family and friends who have been by my side throughout my entire Master’s journey. Their support, love and continuous encouragement are what kept me motivated and determined to always do my best.

CONTRIBUTORS AND FUNDING SOURCES

Contributors

This work was supervised by Dr. Ahmed Abdel-Wahab and Dr. Marcelo Castier from the Chemical Engineering Program and Dr. Eyad Masad from the Mechanical Engineering Program. The routines for the equation of state used in the development of the process simulator were provided by Dr André Zuber. The parameter fitting routines used in this research work were provided by Dr Marcelo Castier and the calculation of the osmotic pressure routine was developed by Muaz Selam. All other work conducted for the thesis was completed by the student.

Funding Sources

This work was made possible in part by the National Priorities Research Program (NPRP) of Qatar National Research Fund under Grant Number NPRP10-1231-160069 and in part by the ConocoPhillips Global Water Sustainability Center (GWSC).

NOMENCLATURE

A	water permeability coefficient
A	Helmholtz energy
A_e	area of the current element
A_m	membrane area
A^{IGM}	Helmholtz energy of the ideal gas mixture
A^R	residual Helmholtz energy
A^{MTC}	Helmholtz energy from the MTC equation of state
A^{Born}	Helmholtz energy calculated from the Born equation
A^{Born}_{disc}	Helmholtz energy calculated from the Born equation for the discharge of ions in a vacuum
A^{Born}_{chg}	Helmholtz energy calculated from the Born equation for the recharge of ions in a dielectric solvent
A^{MSA}	Helmholtz energy from the mean spherical approximation
B	salt permeability coefficient
c_M	molar salt concentration of the mixture
c_A	molar salt concentration of solution A
c_B	molar salt concentration of solution B
$C_{D,m}$	concentration of the draw in the solution-membrane interface

$C_{D,b}$	concentration of the draw solution in the bulk
$C_{F,m}$	concentration of the feed in the solution-membrane interface
$C_{F,b}$	concentration of the feed solution in the bulk
D	diffusion coefficient
E_k	kinetic energy
E_p	potential energy
G_{mix}	Gibbs free energy of mixing
H	enthalpy
J_w	diffusive water flux across the membrane
J_s	salt flux
k	mass transfer coefficient
$\dot{m}_{p,s}$	reverse salt flux
n	number of moles of the species
$\dot{n}$	molar flowrate
n_s^D	molar flowrate of the solute in the draw
n_s^F	molar flowrate of the solute in the feed
n_w^D	molar flowrate of the water in the draw
n_w^F	molar flowrate of the water in the feed
P	hydrostatic/hydraulic pressure
$\dot{Q}$	heat transfer rate

R	salt rejection
R	gas constant
S	structural parameter
S	entropy
T	temperature
U	internal energy
V_D	volumetric flowrate of the draw
V_F	volumetric flowrate of the feed
$\dot{V}_p$	water permeate flowrate
V	volume
$\dot{W}$	power
x_i	mole fraction of species i present in the solution

Greek letters:

π	osmotic pressure
π_D	osmotic pressure of the draw solution
π_F	osmotic pressure of the feed solution
$\pi_{D,b}$	osmotic pressure of the draw solution in the bulk
$\pi_{F,b}$	osmotic pressure of the feed solution in the bulk
η	efficiency
γ_i	activity coefficient

ϕ_A	ratio of the moles of A to the total moles in the solution
ϕ_B	ratio of the moles of B to the total moles in the solution
ν	number of ions each electrolyte molecule dissociates into

TABLE OF CONTENTS

Page

LIST OF FIGURES

Page

LIST OF TABLES

Page

CHAPTER I

INTRODUCTION

Pressure-retarded osmosis (PRO) is a salinity gradient power generation process [1-6], which is based on the mixing of two solutions of different salinities. In PRO, the solvent passes through a semi-permeable membrane from a low salinity feed solution to a highly concentrated draw solution. The draw solution is pressurized and the permeate water flow is retarded by applying a hydraulic pressure difference lower than the osmotic pressure difference [7]. A hydro-turbine is then used to extract the power obtained from the pressurized draw solution. High salinity process waters (e.g. desalination brine, hydrocarbon-produced water) have been favoured [8] as draw streams applicable to the design of potentially viable PRO plants. Produced water represents the largest volume of waste stream in oil production and harnessing the osmotic energy in a PRO process can be used for simultaneously reducing the pumping energy requirements and enhancing injectivity [9]. Commonly used modules for PRO processes are those with plate-and-frame, spiral-wound, tubular, and hollow fiber structures. Spiral-wound modules have been favored in the development of proof-of-concept, pilot-scale plants – such as the GMVP pilot PRO plant in Korea [10]. This is likely due to their high packing density, ease of cleaning, and lower cost [11] relative to other classes of membrane modules. Such spiral-wound modules are fabricated as rolled layers of membrane “leaves”. It is typical to characterize the membrane material of constituent leaves separately, in standard, coupon-scale experiments. Thus, there is a need to bridge the gap between the results of coupon-scale membrane characterization experiments and the performance of plant-scale spiral-wound membrane modules [12, 13]. This is accomplished through a suitable treatment of dilution effects and driving force profiles such that they are consistent with flow patterns within the fabricated structure of the spiral-wound membrane module.

The focus of this line of research is on possible applications that pair streams with more pronounced salinity differences, such as brine discharged from desalination plants with seawater or produced water from oil/gas production with seawater. Such pairings increase the likelihood of finding the conditions for commercially viable processes. In this specific project, a PRO simulator developed in-house is utilized for this purpose.

The solution diffusion model has been widely used [1, 4, 14-16] to describe mass transport across the membrane in PRO processes. These proposed models do not take the spatial variations of hydraulic pressure, velocity, and concentration into account. Therefore, these models cannot be employed for an accurate analysis of different membrane modules with variable concentration profiles and thus variable osmotic pressure difference along the membrane length. The main goal of this research work is to assess the performance of spiral-wound modules in PRO processes with respect to permeate flux and power production. This is achieved by simulating the spiral-wound membrane geometry and analyzing different process conditions in a full-scale high salinity PRO process simulator that incorporates established mass transfer models, an electrolyte equation of state (EoS) for calculation of thermodynamic properties, and process equipment characteristics.

CHAPTER II

LITERATURE REVIEW

Osmotic Processes

Osmotically driven membrane processes (ODMPs) are increasingly becoming a topic of interest and have been cited by National Geographic in an article on April 2010 as one of the three most promising new desalination technologies [17]. The osmosis process requires a selectively permeable membrane that separates two fluids with different osmotic pressures. Natural osmosis is when the fluid of lower osmotic pressure flows across the membrane to dilute the fluid of higher osmotic pressure when both fluids are at the same hydraulic pressure [17]. This process takes place with variations that include pressure enhanced osmosis and pressure retarded osmosis. When the solvent transported in this process is water, then the diffusive water flux (L.m^{-2}.h^{-1}) associated across a membrane interface is given by Equation 1 [17]:

$$J_w = A(\Delta\pi - \Delta P) \tag{1}$$

where, A (L.m^{-2}.h^{-1}.bar^{-1}) is the water permeability coefficient, $\Delta\pi$ (bar) is the osmotic pressure difference between the feed and draw sides of the membrane and ΔP (bar) is the applied hydraulic pressure difference [17]. Lee et al. characterized the various osmotic processes as follows [18]:

1. Forward Osmosis (FO): $\Delta P = 0$. Water permeates from the region of lower salinity to that of higher salinity – driven by their difference in osmotic pressure;

2. Pressure Retarded Osmosis (PRO): $0 < \Delta P < \Delta\pi$. Water permeates from the region of lower salinity (PRO feed) to that of higher salinity (PRO draw) – inhibited somewhat by the relatively higher pressure at the draw side;
3. Reverse Osmosis (RO): $\Delta P > \Delta\pi$. Water permeates from the region of higher salinity to that of lower salinity – induced by an applied hydraulic pressure difference working against and exceeding the difference in osmotic pressure.

Figure 1 summarizes the characterization of the different osmotic processes. It shows that the solvent (water) moves from the feed solution to the draw solution in forward osmosis and pressure retarded osmosis.

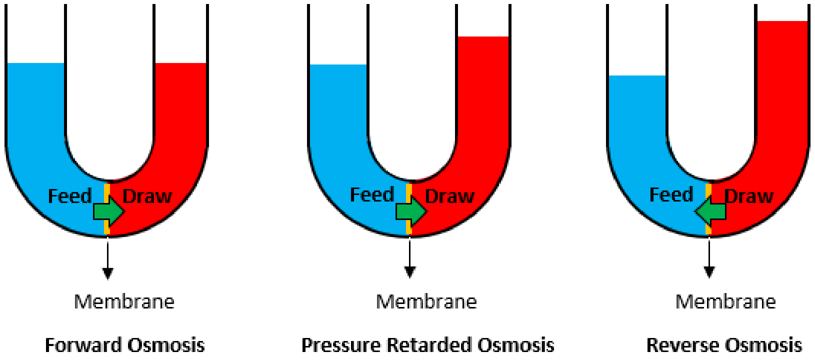

Figure 1: Characterization of the different osmotic processes

Spiral-wound membranes

Modules Configuration

Spiral wound (SW) modules consist of several flat-sheet membranes, spacers and porous permeate flow material that are wrapped around a central tube. According to Lien, the use of multiple membrane leaves results in an effective membrane area higher than that of a module that consists of a single leaf [19]. The ends of the tube are open to allow the feed solution to flow in and out [11]. A spiral wound module contains a glue line, which forces the feed solution through the feed channel and thus enhances the water permeation between the feed and draw solutions [11]. The permeate flows through the membrane is cross flow to the feed solution and towards the central collecting tube [19]. The tube is sealed at the center and the spiral wound element is then placed inside a pressure vessel [11]. Spiral wound membrane modules are commonly used in membrane separations since an appropriate feed side spacer can provide a relatively high feed side mass transfer coefficient [19]. However, the permeate back pressure associated with using spiral-wound modules is considered a significant issue [19]. A permeate spacer with low pressure drop characteristics can be incorporated to reduce the effects of the permeate back pressure. The configuration of a typical spiral-wound element is illustrated in Figure 2 [11].

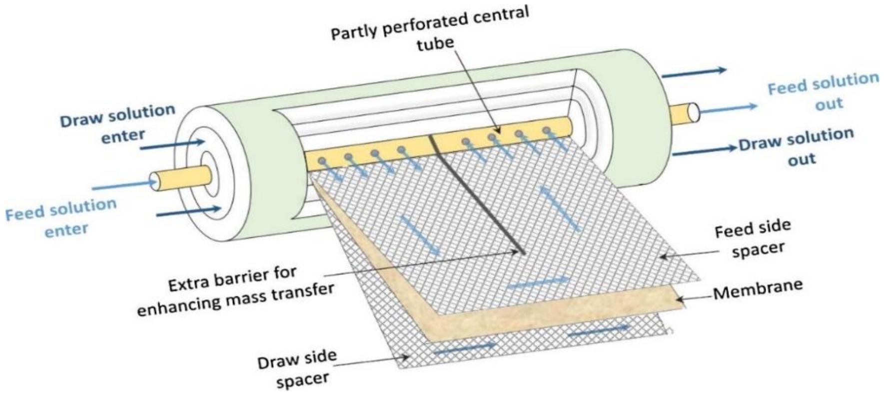

Figure 2: Spiral-wound membrane, Reprinted with permission from [11]. Copyright 2016 Elsevier

PRO studies

Most existing PRO studies on membranes or process configurations focus on small-scale membrane coupons [12]. Although these types of studies are crucial as they help in gauging the relative performance of different membranes, they do not represent an accurate representation of the viability of PRO [12]. The energy output and efficiency of the full-scale process must be studied to be able to verify the overall viability of PRO [12]. Very few studies have been carried out to investigate PRO in large-scale due to the difficulty of constructing and operating these systems [12]. A PRO pilot plant built in Norway used cellulose acetate membranes to generate a power density of less than 0.5 W per square meter of membrane area [13]. This power density is an order of magnitude lower than that required to make the process viable (5 Wm^{-2}) [13]. In order to bridge this gap, membranes need to be tailored such that the support layer decreases internal concentration polarization (ICP), which is when the solvent (usually water) permeates through the support and dilutes the draw concentration at the active layer’s inner side [13, 20]. ICP can lower the water flux obtainable dramatically and thus it is crucial to study these factors in PRO processes [20].

Straub et al. [21] analyzed the extractable power for different pairings including seawater and river water. Their study showed that any additional energetic input (e.g., pre-treatment, pumping) into a PRO process will reduce the efficiency of energy conversion significantly [21]. They concluded that pairings with hypersaline waters as draw solution must be studied to determine the viability of PRO processes.

Kim et al. [7] carried out an experimental analysis using a prototype 8040 PRO membrane (8-in. by 40-in.) to examine the relationships between pressures, flow rates, and salinity gradients in a spiral-wound module. Their study concluded that the reduction in the net energy generation can be attributed to the flow resistance and shadow effect of the spacers used within the feed channel of the spiral-wound membrane module. [7] They also showed that a higher inlet draw pressure is required in order to maintain the desired pressure difference across the membrane since a higher inlet feed pressure is necessary to make up for the pressure losses that take place in the feed channel. [7] In order to prevent membrane deformation, Kim et al. used dense tricot fabric spacer which caused the pressure losses through the test module to exceed model predictions. [7] They stated that the high experimental pressure losses in the feed channel reduced the efficiency of the spiral-wound module significantly. [7]

Achilli et al. [22, 23] have also carried out an experimental study to analyze the energy lost in processes internal to the PRO module. Achilli et al. used a 4040 spiral-wound membrane module (4-in. by 40-in.) to show that with higher cross-flow velocities, power densities above 8 W/m^2 could be achieved. However, their study also showed that the pumping energy required to overcome the pressure losses along the module resulted in a negative overall net specific energy. [22, 23]

Previous studies have shown that the PRO performance highly depends on whether the active layer is faced by the draw solution (ALDS mode) or by the feed solution (ALFS mode) [11]. These studies showed that a better performance is obtained in the ALDS mode [11]. When the ALDS mode is used in spiral-wound membranes, the feed circulates through the perforated central tube and spreads inside the membrane envelope via a feed spacer. On the other hand, the draw solution circulates outside the membrane envelope through the use of a permeate spacer [11].

A PRO modeling and experimental study was previously carried out by Attarde et al. [11] using a commercially available spiral wound FO membrane module. They used a thin film composite (TFC) polyamide membrane which is consisted of an active area equivalent to 0.24 m^2 that was wound to take a spiral-wound form. However, it is important to note that this membrane was not strong enough to achieve power production at high hydraulic pressures for PRO, as it could only sustain a maximum hydraulic pressure of 5 bars [11].

Previous studies used solution-diffusion (SD) based models to describe the mass transfer across the membrane but this model does not take into account the convective phenomena in mass transport [11]. The mass transport can also be described by irreversible thermodynamic models that are based on linear relations between fluxes and driving forces when the system is close to an equilibrium state or by the Spiegler-Kedem (SK) model [11]. The SK model is a mass transfer model that relates flux to a solute’s concentration difference. The experimental data of flux versus rejection for individual ions of different membranes were used to validate the model. The predictions obtained from the SK-based model were close to the experimental results, especially when the hydraulic pressures of the draw solution were low [11]. The study also concluded that more studies are needed to improve the support layer of the membrane, type of the spacers, and the thickness and strength of the glue line, as these factors are crucial in the design and analysis of a commercial scale unit [11]. The conclusions from that study were that a higher energy extraction efficiency is obtained at lower flow rates of the feed and draw solutions and can be enhanced by optimizing operational parameters such as the length to width ratio of the membrane [11].

There are two different flow paths in the spiral wound membrane module, axial and spiral [7]. Additionally, there are two different types of spacers, net and tricot, for the draw and feed solution streams [7]. The relationship between two interacting flow streams in a prototype SW PRO membrane module, and the effect of using a tricot fabric spacer as a feed spacer on the PRO performance was investigated by Kim et al. [7]. The presence of the tricot spacer inside the membrane envelope resulted in a pressure drop due to flow resistance and a lower osmotic water permeation [7]. For a 0.6 M NaCl solution and tap water, the water flux and corresponding maximum power density obtained in this study were 3.7 Lm^{-2} h^{-1} and 1.0 Wm^{-2}, respectively, when the hydraulic pressure difference was 9.8 bar [7]. That study concluded that the thickness and porosity of the tricot spacer should be optimized for better performances of PRO SW modules [7].

A PRO process simulator was previously developed by Manzoor et al.[24, 25] and validated for flat-sheet membranes through comparisons with published literature data. The simulator uses the Q-electrolattice equation of state to predict thermodynamic properties of high salinity solutions and the osmotic pressures of the NaCl solutions while taking dilution effects into account [26]. This is important for plant scale simulations, which this work aims to address. The PRO process simulator can be used for bench scale and full-scale simulations, with user-specified equipment efficiencies and different flow configurations [24, 25]. The PRO simulator uses Yip et al.’s [27] model equations for estimating the water and salt fluxes with the Q-electrolattice equation of state. The PRO process simulator was developed further in this work, to model the spiral-wound membranes’ complex geometry and evaluate their performance with regards to power production for different process conditions.

CHAPTER III

METHODOLOGY

This work was developed in the context of a long-term research project whose ultimate goal is to assess and compare different configurations for the PRO processes. The specific contribution of this thesis is a new procedure to simulate/design spiral wound membrane units, formulated and programmed in such a way that it could be incorporated in the PRO simulator that has been developed by Manzoor et al.[24, 25]. Thus, to provide proper perspective, this chapter initially summarizes the features of this simulator before providing details about the modeling of spiral wound membrane units.

PRO Simulator

An existing simulator for PRO processes that has been developed by Manzoor et al. [24, 25], and previously validated for flat-sheet membranes, was extended in this research work to model the performance of spiral-wound membranes. Using a graphical interface [24], the user specifies the properties of input streams to the process, configuration of the pumps, turbines, pressure exchangers, stream mixers, stream splitters, and membrane modules that comprise the process. A schematic of the simulated PRO process is illustrated in Figure 3.

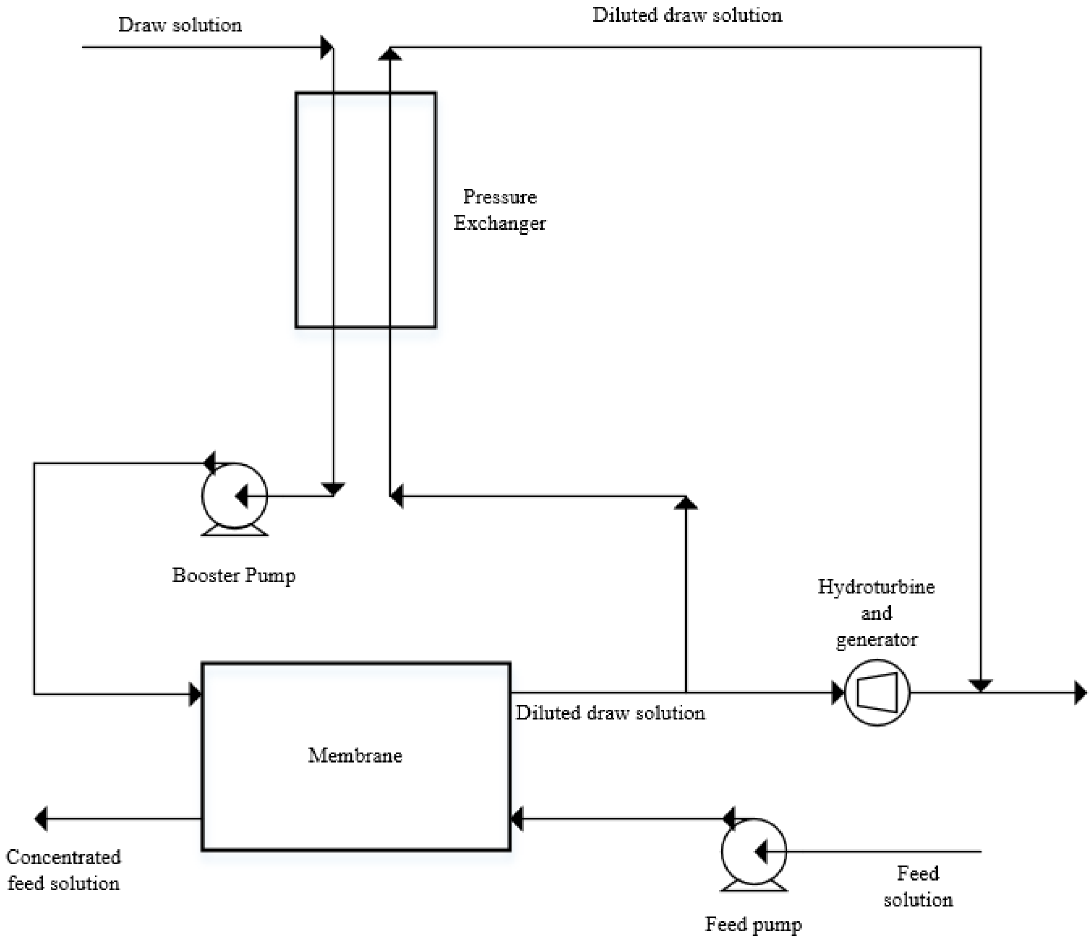

Figure 3: PRO process schematic, Reprinted with permission from [24]. Copyright 2019 Elsevier

Each of these pieces of equipment is implemented as a module in such a way that, for known input stream conditions and applicable assumptions and operational parameters, the module predicts the output stream conditions and the target operational parameters. Details about specific equipment modules and utilized thermodynamic models are presented in previous publications [24, 25]. Predicting the thermodynamic properties of high salinity solutions accurately with a general model while considering dilution effects that is important for plant scale simulations remains an open problem in the scientific literature [12, 24, 28-30]. A key feature that distinguishes our approach from those that have been reported in the literature is the utilization of a detailed thermodynamic model that incorporates an electrolyte sophisticated equation of state for osmotic pressure calculations rather than using simple models, such as van’t Hoff equation. Examples of equations of state for electrolyte solutions include the ePC-SAFT [31], eSAFT – VR Mie [32], e-CPA [33], and the Q-electrolattice [34] equation of state, which is the equation of state used in this work. The advantages of using Q-electrolattice are: 1) it is simpler to use than the other equations of state mentioned, 2) parameters are available for the cations and anions needed to simulate PRO processes, and 3) the results generally are as good as those of the other EoS mentioned.

Model Development

Membrane Module

The Q-electrolattice equation of state is used in the current PRO simulator, which was developed and used by Manzoor [24]. The current PRO simulator retains the use of the Q-electrolattice equation of state. The equation of state parameters were optimized against osmotic coefficients and liquid densities to achieve more accurate predictions [24]. Several important modules were necessary to code in order to simulate the overall PRO process. These modules include the membrane, pump, turbine, and pressure exchanger. The basis of the membrane model involves the development of the transport and mass balance equations[35]. The transport equations aim to explain the osmotic phenomena that take place due to the membrane and fluid dynamics in the channels [35].

The mass balance equations outline the change in the fluid concentrations along the channels [35]. The water flux (J_w) is a function of all of the following [35]:

1. Osmotic pressure difference between the two channels ($\Delta\pi$)
2. The applied hydraulic pressure (ΔP)
3. The fluid dynamics in the draw solution channel
4. The salt diffusivity in the porous support of the membrane
5. The three membrane characterization parameters: water permeability (A), salt permeability (B) and the structural parameter of the porous support layer (S).

Equation 2 represents the water flux as a function explicit in bulk phase osmotic pressures at the feed ($\pi_{F,b}$) and draw ($\pi_{D,b}$) sides of the membrane [35].

$$J_w = A\left[\frac{\pi_{D,b}\, exp\left(-\frac{J_w}{k}\right) - \pi_{F,b}\, exp\left(\frac{J_w\, S}{D}\right)}{1 + \frac{B}{J_w}\left\{exp\left(\frac{J_w\, S}{D}\right) - exp\left(-\frac{J_w}{k}\right)\right\}} - \Delta P\right] \tag{2}$$

In Equation 2, k (L.m^{-2}.h^{-1}) is the membrane mass transfer coefficient, S (m) is the structural parameter of the support layer, D (m^2.s^{-1}) is the bulk diffusion coefficient and B (L.m^{-2}.h^{-1}) represents the salt permeability coefficient.

Undesired phenomena such as external and internal concentration polarization that impact the process performance are represented by Equations 3 and 4, where C is the salt concentration in what units [35].

$$C_{D,m=}\ C_{D,b}\exp\left(\frac{-J_w}{k}\right)-\frac{B}{J_w}(C_{D,m}-C_{F,m})\left[1-\exp\left(\frac{-J_w}{k}\right)\right] \tag{3}$$

$$C_{F,m=}\ C_{F,b}\exp\left(\frac{J_wS}{D}\right)+\frac{B}{J_w}(C_{D,m}-C_{F,m})\left[\exp\left(\frac{J_wS}{D}\right)-1\right] \tag{4}$$

The salt flux J_s (mol.m^{-2}.h^{-1}) is then determined by equation 5 where the concentration difference is obtained by substituting in equations 3 and 4 [35]. The salt fluxes are evaluated as functions of the feed ($C_{F,b}$) and draw ($C_{D,b}$) bulk phase concentrations in mol.L^{-1}.

$$J_s = B(C_{D,m}-C_{F,m}) = B\left[\frac{C_{D,b}\,exp\left(-\frac{J_w}{k}\right)-C_{F,b}\,exp\left(\frac{J_w\,S}{D}\right)}{1+\frac{B}{J_w}\left\{exp\left(\frac{J_w\,S}{D}\right)-exp\left(-\frac{J_w}{k}\right)\right\}}\right] \tag{5}$$

The water permeate flowrate $\dot{V}_p$ (L.hr^{-1}) is calculated through the integration of J_w over the area of the membrane A_m (m^2) :

$$\dot{V}_p = \int_0^{A_m} J_w da \tag{6}$$

The molar volume of the solution obtained by the Q-electrolattice EoS is used to convert the volumetric flowrate of water into its corresponding molar flowrate.

The reverse salt molar flowrate (mol.s^{-1}) for a full-scale membrane is given by Equation 7.

$$\dot{m_{p,s}} = \int_0^{A_m} J_s da \tag{7}$$

The assumptions made in the modelling of the membrane unit were as follows [24]:

- The membrane unit operates isothermally.

- The pressure drop along each side of the membrane unit is user-specified.

The integration of these equations has to be done numerically because of the flow patterns of the draw and feed streams inside the spiral-wound module and because the fluxes depend on position within the unit in a sophisticated way. In fact, the flux equations, which are explicit in the osmotic pressures of saline feed and draw streams, must also be evaluated in conjunction with a suitable thermodynamic model (e.g., an EoS) applicable to aqueous electrolytes.

The process simulator used in this work deploys the Q-electrolattice EoS to calculate bulk phase osmotic pressures at the draw and feed sides of the membrane, as well as the thermodynamic state properties of process streams (which are inputs to the various equipment models implemented within the process simulator) [24, 25]. The salinities of draw and feed inlet streams are specified as inputs to the process simulator.

The simulator was previously developed for flat-sheet membranes using a one-dimensional model as shown in Figure 4.

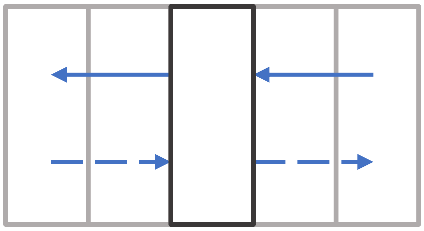

Figure 4: One-dimensional model

However, for the modeling of the spiral-wound membranes an extension of the model to a 2-dimensional basis was necessary. The proposed 2D formulation for the unrolled spiral-wound membrane discretization is illustrated in Figure 5 [28]. The red flow patterns represent the draw inlets and outlets respectively; whereas, the blue arrows are representative of the feed solution flow pattern, which is impacted by the central glue-line (illustrated by the yellow line in Figure 5). The black nodes that are located at the draw and feed inlets are used as boundary conditions. The upper right-most element, which has three black nodes as its vertices, has known values for the thermodynamic properties such as pressure and temperature, since it is located at the intersection between the feed and draw inlets.

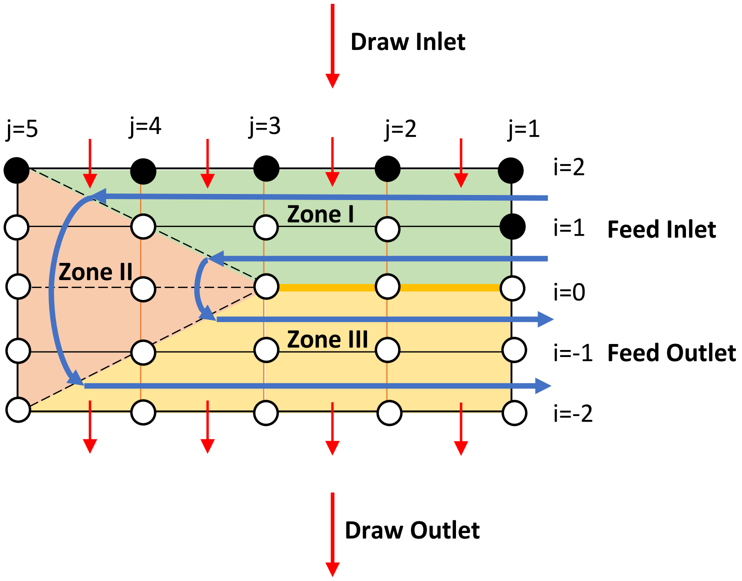

Figure 5: Discretization of the unrolled spiral-wound membrane [28]

The 2D formulation was programmed such that the correct flow connectivity between discretized grid elements is established in an automated, generalized fashion consistent with the user-specified level of discretization and fractional length of the central glue-line (which itself provokes the flow of the feed stream in the membrane leaf). Flow connectivity between grid elements imposes an element-wise sequence on the recursive flux calculation/material balance performed on each element. Elements are classified according to the location of their vertices. Depending on the location of the grid element (i.e. “Zone” I, II or III), the element-specific flow directions of the feed and draw streams can be described as either cross-flow (Zones I and III) or co-current flow (Zone II). For the elements that are located partially in Zones I and II/ Zones II and III, the feed solution inputs and outputs were classified according to the flow connectivity between the grid elements. Thus, for the elements that are partially located in Zones I and II, the feed input was specified as the feed output of the previous element (located to the right of the current element) and the feed output was specified as the feed input of the subsequent element (located underneath the current element). As for the elements that are partially located in Zones II and III, the feed input was taken to be the feed output of the previous element (located above the current element) and the feed output of the current element was specified as the feed input to the subsequent element (located on the right of the current element). The draw solution flows in the plane of the draw-side spacer. The feed stream flows in the plane of the feed spacer – traversing Zones I-III. Water flux and reverse salt flux are normal to the membrane leaf, which itself is situated between the two spacers. At the membrane inlets, molar flowrates of the external draw and feed streams are “split” equally amongst the number of elements that each stream “sees” as it enters the membrane.

For each element in the 2D discretized membrane unit, the following mass balance equations have to be satisfied:

$$n^{D}_{w,\,previous\ element} + \frac{\int_0^{Ae} J_w da}{V_m * 3600*1000} = n^{D}_{w,\,current\ element} \tag{8}$$

$$n^{D}_{s,\,previous\ element} - \frac{\int_0^{Ae} J_s da}{3600} = n^{D}_{s,\,current\ element} \tag{9}$$

$$n^{F}_{w,\,previous\ element} - \frac{\int_0^{Ae} J_w da}{V_m * 3600*1000} = n^{F}_{w,\,current\ element} \tag{10}$$

$$n^{F}_{s,\,previous\ element} + \frac{\int_0^{Ae} J_s da}{3600} = n^{F}_{s,\,current\ element} \tag{11}$$

where n^D and n^F represent the draw and feed molar flowrates in mol.s^{-1} respectively. The water and salt fluxes in equations 8-11 are in L.m^{-2}.h^{-1} and mol.m^{-2}.h^{-1} respectively. A_e represents the area of the current element in m^2 and V_m represents the molar volume of the solution in m^3.mol^{-1} given by the EoS at the solution's temperature and pressure. The species represented in these equations are the solute (s) and water (w) in the draw and feed streams. The mass transfer equations are solved sequentially for each discretized membrane element using boundary conditions that are determined by the feed and draw inlet streams and a sufficient step size.

The feed and draw side flowrates at the membrane inlets, equations 8-11, and the mass transfer model equations 2,5 are solved simultaneously over discrete elements. This allows the simulator to capture the effects of continuous dilution on the thermodynamic properties across the membrane area.

After having completed the numerical integration of the flux equations along the entire area of the membrane leaf, the previously “split” feed and draw streams are aggregated at their respective membrane outlets. The thermodynamic properties of the reconstituted streams are then calculated through an adiabatic mixing operation. (Refer to Appendix A for calculation flowchart depicted in Figure 20).

The flat-sheet membrane requires the initialization of these properties using only one draw steam and one feed stream, as shown in Figure 6.

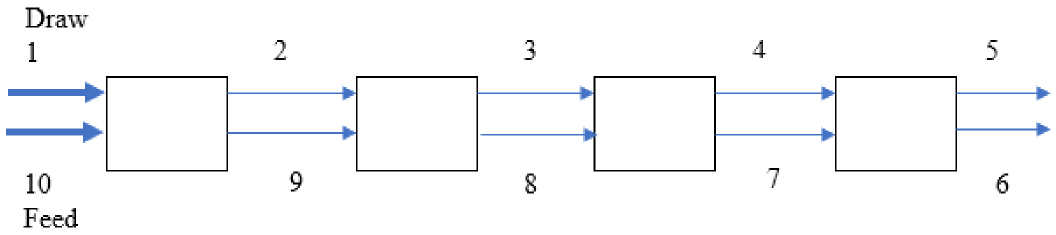

Figure 6: Flat-sheet membrane initialization

In this co-current flat shat membrane example, the draw and feed stream inputs (e.g., streams 1 and 10 respectively) were used to initialize the properties of the flat-sheet membrane. On the other hand, several draw and feed streams were required to initialize the properties in the case of the spiral-wound membrane. As shown in Figure 7, which illustrates a four-element spiral-wound membrane, 2 draw streams and 1 feed stream were needed for initialization as they correspond to elements that obtain either their draw/feed from the environment.

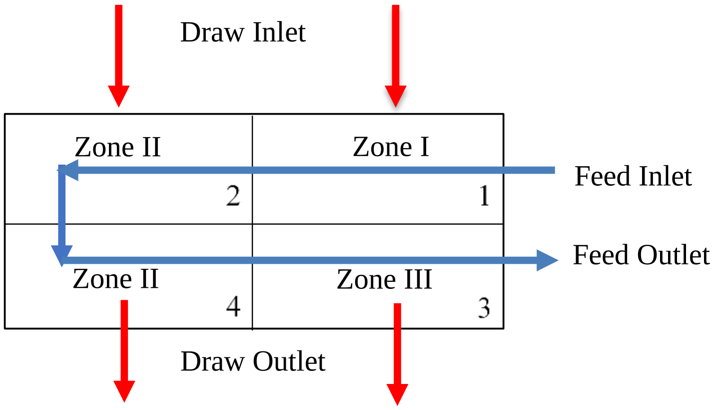

Figure 7: Spiral-wound membrane initialization

Each element in a spiral-wound membrane has two inlet streams and two outlet streams as shown in Figure 7. The draw solution (represented by red arrows in Figure 7) flows across the membrane from Zone I to Zone III and thus the draw outputs of elements 1 and 2 are going to be the draw inputs of elements 3 and 4 respectively. Moreover, the feed solution (represented by blue arrows in Figure 7) flows from Zone I to Zone II and from Zone II to Zone III. Thus, the feed output of element 1 is the feed input to element 2, the feed output of element 2 is the feed input to element 4 and the feed output of element 4 is the feed input to element 3. As can be seen, the draw and feed inputs and outputs are determined by the draw and feed flow patterns. The properties of the draw and the feed streams that leave the membrane are then calculated in the PRO simulator following the flux and osmotic pressure calculations. These calculations are carried out in a similar fashion for the flat-sheet and spiral-wound membranes. However, the sequence of calculations is different for the two membrane types due to the difference in the geometry of the membranes. The pump, turbine and pressure exchanger modules were unchanged and used readily, as they were already previously developed in the flat-sheet membrane simulator [24].

Pump Module

The assumptions that were carried out in the derivation of the pump module include the following [24]:

1. Adiabatic and reversible operation
2. Steady state with no changes in potential and kinetic energy

Based on the assumptions listed above, the energy and entropy balances shown in equations 12 and 13 simplify to equations 14 and 15 respectively [24].

$$\frac{d[\dot{n}(U+E_k+E_p)]_{system}}{dt} = \sum_{in}[\dot{n}(H+E_k+E_p)]_{in} - \sum_{out}[\dot{n}(H+E_k+E_p)]_{out} - P\frac{dV_{system}}{dt} + \dot{Q} + \dot{W}_{shaft} \qquad (12)$$

$$\frac{d[\dot{n}S]_{system}}{dt} = \sum_{in}[\dot{n}S]_{in} - \sum_{out}[\dot{n}S]_{out} + \sum_{sys}\frac{\dot{Q}}{T} + \dot{S}_{gen} \qquad (13)$$

$$\dot{W}_{shaft} = \dot{n}\big(h_{out}(T_{out}, P_{out}, x_{out}) - h_{in}(T_{in}, P_{in}, x_{in})\big) \qquad (14)$$

$$\dot{n}\big(s_{out}(T_{out}, P_{out}, x_{out}) - s_{in}(T_{in}, P_{in}, x_{in})\big) = 0 \qquad (15)$$

The efficiency of the pump is then calculated as follows:

$$\eta_{pump} = \frac{|W'_{shaft,rev}|}{|W_{shaft,real}|} \qquad (16)$$

In Equations 12-16, E_k E_p, H, $\dot{n}$, P, $\dot{Q}$, S, T, U, V, $\dot{W}$, x, η represent kinetic energy, potential energy, enthalpy, molar flowrate, pressure, heat transfer rate, entropy, temperature, internal energy, volume, power, mole fractions and efficiency respectively.

Turbine Module

The derivation for the turbine module was very similar to that developed for the pump [24]. The main difference was that mechanical power is now an output instead of an input [24]. The assumptions are the same as those used for the pump module [24]. The efficiency of the turbine is obtained using Equation 17 [24].

$$\eta_{turbine} = \frac{|W_{shaft,real}|}{|W'_{shaft,rev}|} \tag{17}$$

Pressure Exchanger Module

For the pressure exchanger module, the depressurization side is modelled in a manner similar to that of a turbine. The power supplied by the depressurization side ($\dot{W}_{depressurization}$) is used to determine the unknown output pressure for the pressurization side.

The assumptions that were used in the derivation of the pressure exchanger module are as follows [24]:

1. a fraction η of the power supplied by the depressurization side is used for the compression of the fluid on the pressurization side
2. The remaining portion, $(1 - \eta_{LP})\dot{W}_{depressurization}$, is assumed to be lost in the form of heat due to friction

The derivation yields Equations 18-21 [24]:

$$\dot{S}_{gen} = \frac{\dot{Q}}{T} \tag{18}$$

$$\dot{Q} = (1 - \eta) * \left|\dot{W}_{depressurization}\right| \tag{19}$$

$$\dot{H_{out}} = \dot{H_{in}} + \left|\dot{W}_{depressurization}\right| \tag{20}$$

$$\dot{S}_{out} = \dot{S_{in}} + \frac{(1-\eta)*\left|\dot{W}_{depressurization}\right|}{T} \tag{21}$$

The symbols represent the same properties as those previously mentioned for the pump module. T in equations 18 and 21 is the average temperature of the inlet and outlet streams on the pressure exchanger's pressurization side.

Simulator Inputs and Outputs

The current version of the simulator includes both the flat-sheet and spiral-wound membrane modules. The necessary inputs required for the simulator to calculate the outputs which are the power density, water and salt flux are shown in Table 1 [24].

Table 1: Simulator Inputs [24]

Inputs	**Units**
Draw solution salinity	g/L
Draw solution pressure	Pa
Draw solution flow	m^3/s
Feed solution salinity	g/L
Feed solution pressure	Pa
Feed solution flow	m^3/s

Table 1 Continued:

Inputs	Units
Membrane water permeability (A)	$Lm^{-2}h^{-1}bar^{-1}$
Membrane salt permeability (B)	$Lm^{-2}h^{-1}$
Membrane mass transfer coefficient (k)	$Lm^{-2}h^{-1}$
Membrane structural parameter (S)	m
Membrane area	m^2
Draw solution membrane pressure loss	Pa
Feed solution membrane pressure loss	Pa
Temperature	K
Total pump efficiency	%
Total turbine efficiency	%
Pressure exchanger, depressurization efficiency	%
Pressure exchanger, pressurization efficiency	%

A and B are determined experimentally using the following procedure which is commonly cited in literature [7]. An RO experiment using tap water as the feed solution was carried out to determine A [7], where the membrane module was compacted with tap water at an applied hydraulic pressure of 19.7 bar. This was done over a time period of 15 h during which the water permeate flow rate was recorded at applied pressures ranging from 3.9 to 19.7 bar [7]. Dividing the water permeate rate by the effective membrane area yielded the water flux (J_W) [7]. The A value was then determined in the experimental study using Equation 22 [7]:

$$A = \frac{J_w}{\Delta P} \tag{22}$$

The salt permeability coefficient (B) was also obtained experimentally in literature by using 2922 mg/L of 0.05 M NaCl solution at different hydraulic pressures [7]. The hydraulic pressures applied were 7.8, 11.7, and 15.7 bar [7]. The B value was then calculated in the experimental study by Equation 23 [7]:

$$B = A * (\Delta P - \Delta\pi)(\frac{1-R}{R}) \tag{23}$$

where R is the salt rejection that is obtained by measuring the bulk feed and permeate solutions' conductivities [7].

The simulator can also be used to calculate the Gibbs free energy of mixing, which is the maximum reversible work that can be obtained when two solutions of different compositions are mixed [27] at constant temperature and pressure. In this work, the Gibbs free energy of mixing is calculated by using the Q-electrolattice equation of state which was implemented in the PRO simulator. The Q-electrolattice equation of state used in the process simulator is an ion-based equation of state, which was developed by using the approach presented by Myers et al. for the calculation of the Helmholtz energy [36]. The Q-electrolattice equation of state was developed based on three different models: Born equation, Mean Spherical Approximation (MSA), and Mattedi–Tavares–

Castier (MTC) equation of state [37]. The Born equation estimates the change in Helmholtz energy by accounting for the discharge of ions in a vacuum (ΔA_{disc}^{Born}) and the recharge in a dielectric solvent (ΔA_{chg}^{Born}) [37]. The Mean Spherical Approximation term takes into account the long-range electrostatic interactions among the ions in an electrolyte solution, whereas the MTC equation of state describes the short-range attractive dispersion and repulsive forces [37]. The residual Helmholtz energy for an electrolyte solution can be obtained as follows.

$$A(T,V,n) = A^{MTC}(T,V,n) + \Delta A^{Born}(T,V,n) + \Delta A^{MSA}(T,V,n) \quad (24)$$

where,

$$A^{MTC}(T,V,n) = A^{IGM}(T,V,n) + \Delta A^{MTC}(T,V,n) \quad (25)$$

$$\Delta A^{Born}(T,V,n) = \Delta A_{disc}^{Born}(T,V,n) + \Delta A_{chg}^{Born}(T,V,n) \quad (26)$$

Replacing equation 25 in equation 24 yields equation 27 as follows:

$$A(T,V,n) - A^{IGM}(T,V,n) = \Delta A^{MTC}(T,V,n) + \Delta A^{Born}(T,V,n) + \Delta A^{MSA}(T,V,n) = A^{R} \quad (27)$$

T represents the temperature of the system, V is the volume, n is the number of moles of the species, A^{IGM} is the Helmholtz energy of the ideal gas mixture which corresponds to the reference state and A^{R} is the residual Helmholtz energy. The term A^{MTC} accounts for the contribution of the MTC equation of state including the ideal gas contribution, whereas ΔA^{MTC} is without the ideal gas contribution [37].

The Q-electrolattice EoS used in the development of the process simulator calculates the residual Helmholtz energy function based on the temperature, pressure and composition of the ions in the solution. Once the Helmholtz energy function is generated, various derivatives are used to calculate the chemical potentials of the ions thereby which, the EoS generates fugacity coefficients and residual properties such as residual entropy and residual enthalpy can then be calculated. The Gibbs free energy of mixing was also calculated using the Q-electrolattice equation of state and it is the total enthalpy of the solution minus the product of the temperature and the total entropy of the solution.

The Gibbs free energy of mixing can also be calculated by using activity coefficient models. Even though this method is not adopted in this project, the derivation required to obtain the Gibbs free energy of mixing is explained further as the resultant equation will be referred to in the subsequent sections.

The change in Gibbs free energy of mixing, which is given by the difference of the final Gibbs free energy of mixing of the mixtures and the initial Gibbs free energy of solutions A and B can be represented by Equation 28 [27].

$$-\Delta G_{mix} = RT * \{[\sum x_i * \ln(\gamma_i x_i)]_M - \phi_{\mathrm{A}}[\sum x_i * \ln(\gamma_i x_i)]_A - \phi_{\mathrm{B}}[\sum x_i * \ln(\gamma_i x_i)]_B\} \quad (28)$$

where x_i represents the mole fraction of species i present in the solution, R is the gas constant, and T represents the temperature. γ_i is the activity coefficient which takes into account the behavior of nonideal solutions [27]. ϕ_{A} and ϕ_{B} are the ratios of the moles of A or B to the total moles in the solution [27]. The mole fraction and the activity coefficient can be approximated to unity in the presence of low salt concentration solutions [27]. Equation 28 then simplifies to Equation 29 where ν is the number of ions each electrolyte molecule dissociates into [27]:

$$\frac{-\Delta G_{mix}}{\nu RT} = [x_s * \ln(\gamma_s x_s)]_M - \phi_{\mathrm{A}}[x_s * \ln(\gamma_s x_s)]_A - \phi_{\mathrm{B}}[x_s * \ln(\gamma_s x_s)]_B \qquad (29)$$

where s represents salt that has dissociated completely in the solution. The mole fraction and molar mixing energy in Equation 29 were converted to molar salt concentration and Gibbs free energy of mixing per unit volume in Equation 30 for practicality purposes [27]. The assumptions made were that the volume of the system remains the same and that the volumetric and mole contribution of the salt to the solution is negligible [27].

$$\frac{-\Delta G_{mix}}{\nu RT} = c_M * \ln\left(\gamma_{s,M} c_M\right) - \Phi c_A * \ln\left(\gamma_{s,A} c_A\right) - (1-\Phi) c_B * \ln\left(\gamma_{s,B} c_B\right) \qquad (30)$$

Multiplying Equation 30 by V_M/V_A ($\approx 1/\phi$) yields the Gibbs free energy of mixing per unit volume of A (the more dilute solution), which would more accurately capture the available energy [27].

$$\frac{-\Delta G_{mix}}{\nu RT} = \frac{c_M}{\Phi} * \ln\left(\gamma_{s,M} c_M\right) - \mathrm{c}_A \ln\left(\gamma_{s,A} c_A\right) - \frac{(1-\Phi)}{\Phi} c_B \ln\left(\gamma_{s,B} c_B\right) \qquad (31)$$

For further simplification, ideal behavior can be assumed and the activity coefficients can be neglected [27].

$$\frac{-\Delta G_{mix}}{\nu RT} = \frac{c_M}{\Phi} * \ln c_M - \mathrm{c}_A \ln c_A - \frac{(1-\Phi)}{\Phi} c_B \ln c_B \qquad (32)$$

The form found in equation 32 will be referred to by the simplified form in the results section.

CHAPTER IV

RESULTS

This section covers the validation of the PRO process simulator results through comparisons with published experimental data. The performance of the spiral-wound membranes has also been analyzed in terms of power production and compared with that of the flat-sheet membranes. Sensitivity analysis was carried out on the spiral-wound implementation in order to identify the sufficient level of discretization and the effect of the glue-line fractional length on the extractable power density.

Gibbs Free Energy of Mixing

The Gibbs free energy of mixing was calculated using the simplified form and the Q-electrolattice equation of state for the following different mixtures:

1. Seawater (0.6 M NaCl) – River Water (0.015 M NaCl)
2. Seawater (0.6 M NaCl) – Brackish Water (0.05 M NaCl)
3. Brine (1.2 M NaCl) – Brackish Water (0.05 M NaCl)
4. Brine (1.2 M NaCl) – Wastewater (0.015 M NaCl)
5. Produced Water (2.74 M NaCl) – Seawater (0.6 M NaCl)

The Gibbs free energy of mixing was plotted against phi (ϕ) where ϕ= (initial volumetric flowrate of feed)/(initial volumetric flowrate of feed + initial volumetric flowrate of draw). The obtained plots using both the simplified form (refer to equation 32) and the Q-electrolattice equation of state can be seen in Figures 8 and 9.

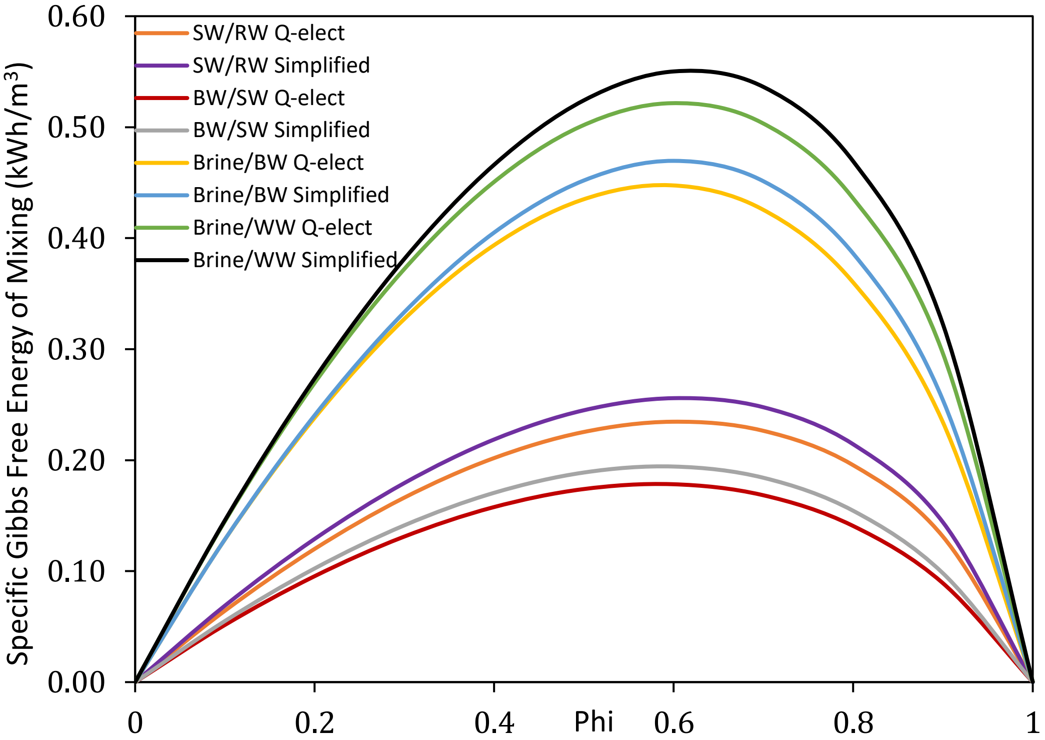

Figure 8: Effect of Φ on the Gibbs energy of mixing for mixtures 1-4 at 298.15 K

In Figure 8, the simplified form is overpredicting the Gibbs free energy of mixing compared to the Q-electrolattice equation of state. The difference between the Gibbs free energy of mixing from the simplified form and the Q-electrolattice equation of state is not large for all the mixtures (mixtures 1-4). The maximum Gibbs free energy of mixing is obtained at a Φ value of about 0.6, which agrees with literature.[21]

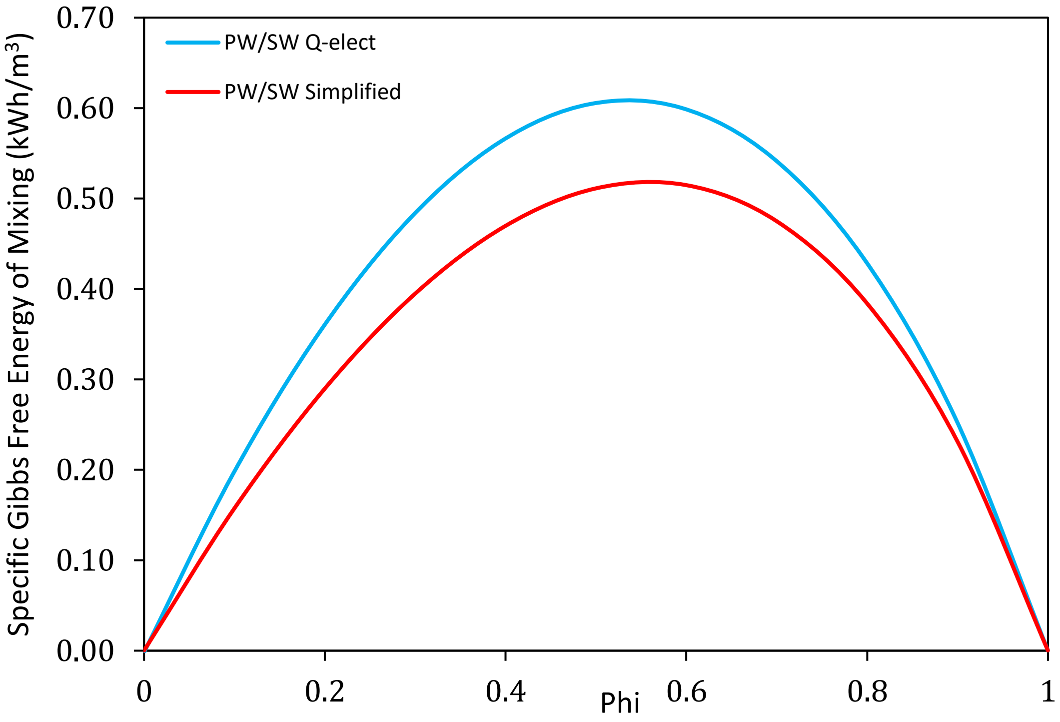

Figure 9: Effect of Φ on the Gibbs energy of mixing for mixture 5 at 298.15 K

However, in Figure 9, the difference in the Gibbs free energy of mixing between the simplified form and the Q-electrolattice equation of state is more pronounced for the produced water-seawater mixture. Additionally, the Φ at which the maximum Gibbs free energy is obtained shifts from the 0.6 value that was seen earlier to a value between 0.5 and 0.6. These discrepancies are most likely related to the ideal solution assumption adopted in the simplified form, which does not hold well for concentrated electrolyte solutions.

Validation of Process Simulator Results

The simulated PRO process that was used to obtain the results in this section is illustrated in Figure 10. The simulator allows the use of pressure exchangers as shown in Figure 3; however, the simplified process in Figure 10 was used in this section to focus on the results of the membrane units, since all rotating equipment were assumed to operate at 100% efficiency.

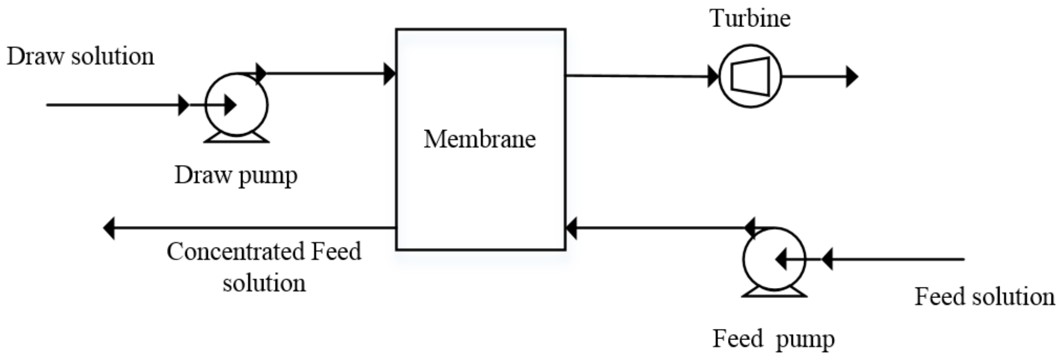

Figure 10: Simplified PRO process schematic, Reprinted with permission from [24]. Copyright 2019 Elsevier

The spiral-wound implementation was validated through multiple different comparisons. For the first of such comparisons, the simulator was run with the several flat-sheet membrane units interconnected with a flow pattern among them that mimics the flow pattern of a discretized spiral-wound membrane unit. The power density and water flux values after the last element of the flat-sheet configuration were then compared with those obtained using the spiral-wound implementation. The results were in complete agreement, which confirmed that the feed and the draw flow patterns were implemented as observed in Figure 5. For example, using the conditions in Table 2 with 8.33×10^{-6} $m^3.s^{-1}$ for the feed (pure water) and draw streams (0.5 M NaCl), with a spiral-wound membrane area that was split in four elements, the calculated power density and water flux at a hydraulic pressure difference of 6.2 bars were equal to 1.6 $W.m^{-2}$ and 9.3 $L.m^{-2}.h^{-1}$, respectively.

Table 2: Specifications for Run #1 and Run #2 taken from [38]

Property	**Run #1 Value**	**Run #2 Value**
NaCl Concentration (M)	0.5	1.0
Feed and Draw Inlet Temperature (˚C)	20	
Feed Inlet Pressure (bar)	1.01	
Membrane Area (m^2)	20.02×10^{-4}	
Draw and Feed Flowrate ($m^3.s^{-1}$)	8.33×10^{-6}	
Water permeability, A ($L.m^{-2}.h^{-1}.bar^{-1}$)	1.23	
Salt permeability coefficient, B ($L.m^{-2}.h^{-1}$)	2.62	
Structural parameter, S (m)	6.89×10^{-4}	7.30×10^{-4}
Mass transfer coefficient, k ($L.m^{-2}.h^{-1}$)	310.32	

A sensitivity analysis was carried out using the process simulator to study the change observed in the power density with each additional element. This was carried out to determine how many elements are sufficient to accurately represent a full-scale membrane. The input conditions that were used to obtain the power density values can be observed in Table 3. The pumps and the turbines were assumed to be 100% efficient. When the change in the power density compared to the previous case is less than 1%, then the number of elements was deemed sufficient.

Table 3: Specifications for Sensitivity Analysis Run

Property	**Draw**	**Feed**
NaCl Concentration (M)	4.1	0.6
Feed and Draw Inlet Temperature (˚C)	25	
Pressure (bar)	60	2.15
Membrane Area (m^2)	30	
Flowrate ($m^3.s^{-1}$)	$4.1x10^{-4}$	$3.84x10^{-4}$
Water permeability, A ($L.m^{-2}.h^{-1}.bar^{-1}$)	0.4	
Salt permeability coefficient, B ($L.m^{-2}.h^{-1}$)	0.3	
Structural parameter, S (m)	$7.02x10^{-4}$	
Mass transfer coefficient, k ($L.m^{-2}.h^{-1}$)	138.6	

The percent change in power density with the total number of discretized membrane elements can be observed in Figure 11.

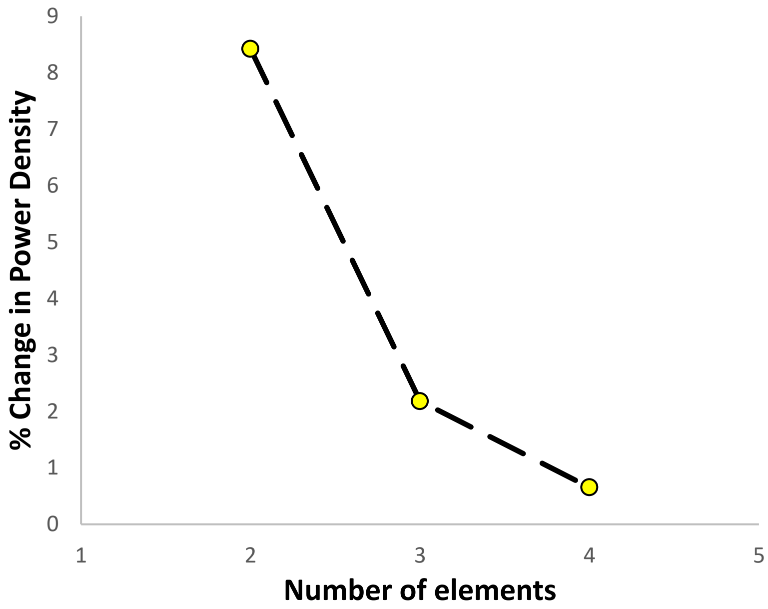

Figure 11: Percent change in power density vs total number of elements

As the total number of elements increases, the percent change in power density decreases. The largest percent change in power density observed was 8%, which was obtained when the total number of elements changed from 1 to 2. The change in power density was less than 1% when the total number of elements changed from 3 to 4. Another criterion that is important to take into consideration is the time needed for the simulation to converge. As the total number of elements increases, the time needed for the simulation to converge also increases. Considering the two criteria specified, 4 discrete elements were deemed sufficient for the examples of this work but the formulation is flexible and can be used with more discrete elements for higher numerical accuracy. In order to obtain higher numerical accuracy for industrial size spiral wound modules, 16 elements were deemed sufficient for this work, as the results obtained from the PRO simulator closely matched those published in literature.

The spiral-wound simulator results were also validated against literature data. Even though the simulator can be used to run cases with high salinities, the validation was carried out using a seawater-freshwater pairing in order to be able to compare the simulator results against the published experimental data [38]. The experimental data reported by Kim et al. [38] was obtained through the use of a flat-sheet FO membrane from Hydration Technology Innovations (HTI). The experiments carried out by Kim et al. utilized NaCl and deionized (DI) water as the draw and feed solutions, respectively. The applied hydraulic pressure differences (ΔP) in those experimental runs were 0.50, 2.92, 6.16, 9.70, and 12.50 bar. The A and B parameters were determined experimentally for the HTI membrane by Kim et al. through the use of DI water and NaCl solution as feed solutions, respectively, in RO mode. The concentrations of the draw and the feed solutions and the permeabilities obtained from the experimental data can be found in Table 2. It is worth mentioning that the experiments carried out by Kim et al. [38] were conducted using low salinity draw solutions due to the PRO test cell limitations.

These conditions were used to generate and reproduce the experimentation results using the spiral-wound simulator. The spiral-wound membrane area was discretized into four elements and the pumps and turbines were assumed to operate at 100% efficiency. The comparisons of the power densities and water fluxes between the experimental and the simulator results are presented in Figure 12 for 0.5 M and 1.0 M NaCl draw solutions.

As Figure 12 shows, there is a close agreement between the power density and water flux values obtained using the simulator and those published in literature.

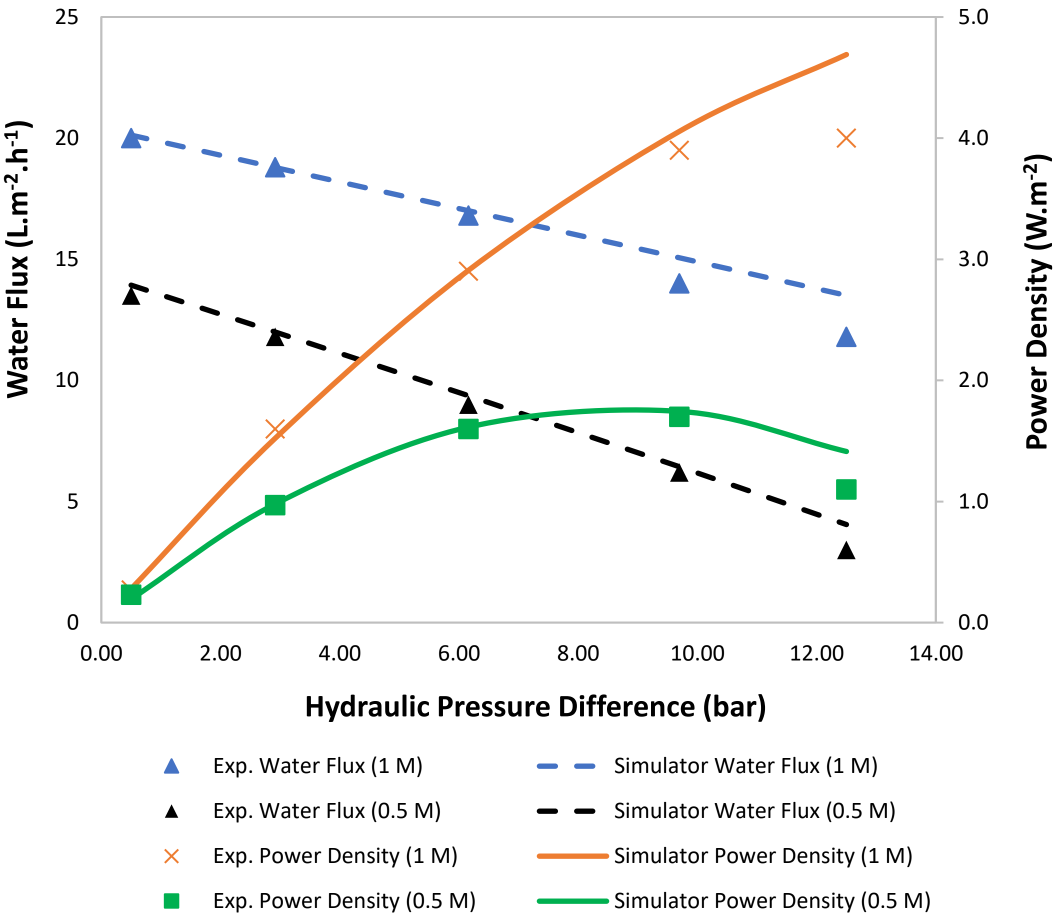

Figure 12: Water flux and power density as a function of applied pressure using an HTI membrane. 0.5 M and 1 M NaCl solution used as draw and deionized water used as feed. Experimental data taken from Kim et al. [38]

The most pronounced deviations occur for operations at the highest hydraulic pressure difference of 12.5 bar, a condition at which small cracks were reported by Kim et al. [38] to be observed on the active layer of the membrane. This possibly caused structural changes to the active and support layers of the membrane and affected the membrane's performance. This most likely explains the differences in results between the simulator and experimental results observed at high hydraulic pressures because our model for membrane units does not account for structural membrane changes.

The spiral-wound simulator results were also validated against experimental data published by Achilli et al., which were obtained for a 4040 spiral-wound TFC PRO membrane module. [39] This validation was carried out using the draw and feed volumetric flowrates and membrane properties reported in the published experimental study, which utilized tap water and 0.48 M NaCl as the feed and draw solutions respectively. [39] Achilli et al. reported power densities for five different draw/feed velocity combinations: 30/38, 30/19, 15/38, 15/19, and 8/6 cm/s. [39] The specifications in Table 4 were used to reproduce the experimental data using the PRO simulator, where the pumps and turbines were assumed to operate at 100% efficiency. [39] The spiral-wound membrane was discretized into 16 elements in order to obtain more accurate results that closely matched with the published experimental data. The comparisons of the power densities between the experimental and the simulator results are presented in Figure 13 for 0.48 M NaCl draw solution with 30/19 and 15/19 cm/s for the draw/feed velocities.

Table 4: Specifications taken from [39]

Property	**Run Value**
NaCl Concentration (M)	0.48
Feed and Draw Inlet Temperature (˚C)	20
Feed Inlet Pressure (bar)	1.01
Membrane Area (m^2)	4.18
Water permeability, A ($L.m^{-2}.h^{-1}.bar^{-1}$)	5.11
Salt permeability coefficient, B ($L.m^{-2}.h^{-1}$)	0.087
Structural parameter, S (m)	$3.10x10^{-4}$

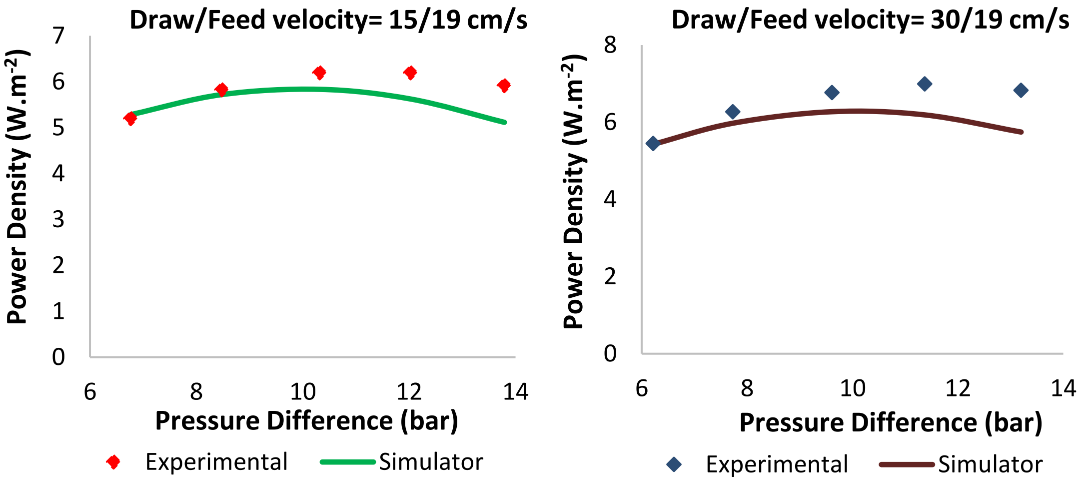

Figure 13: Power density as a function of applied pressure using a 4040 spiral-wound module for different draw/feed velocities. 0.48 M NaCl solution used as draw and tap water used as feed. Experimental data taken from Achilli et al. [39]

As Figure 13 shows, the power density values obtained using the simulator and those published by Achilli et al. are close. The differences in power densities can be attributed to the dynamic nature of the permeability coefficients of the membrane which change with pressure as Achilli et al. have illustrated in their study.[22] A decrease in the water permeability or an increase in the salt permeability can result in a decrease in the peak power density. The permeability coefficients that were reported by Achilli et al (as obtained from the membrane's manufacturer) and used to generate the simulator results are shown in Table 4. [39] Similar trends were obtained for the remaining draw/feed velocity combinations 30/38, 15/38, and 8/6 cm/s which are not shown in Figure 13.

Effect of A and B on Power Density

The effects of altering the water and salt permeability coefficients on the water flux were studied using the PRO simulator and the results are shown in Figure 14.

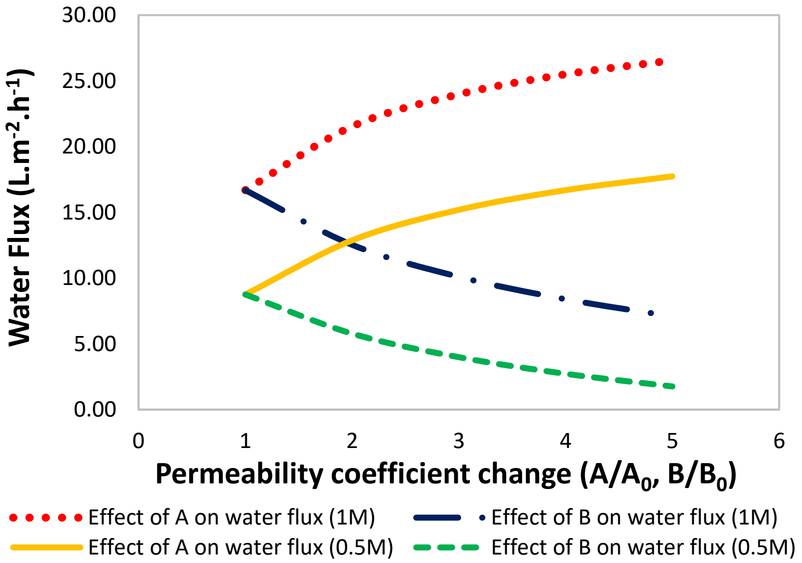

Figure 14: Effect of permeability coefficients on the calculated water flux for a 0.5 M and 1 M NaCl draw solution with deionized water used as feed.

The specifications used to generate Figure 14 are the same as those in Table 2, where the water and salt permeability coefficients reported in the table represent the values used for the base case. The concentrations of the draw solution that were used to generate the results in Figure 14 were 0.5 M and 1 M NaCl. The hydraulic pressure difference was kept constant at 6 bar to solely study the effect of changing the membrane material on the water flux and thus power density.

As shown in Figure 14, an increase in the water permeability coefficient results in an increase in the water flux. For example, for the same $\frac{A}{A_0}$ ratio of 5, the water flux increased by 2.0 times and 1.6 times for a 0.5 M and a 1 M NaCl draw solution concentration, respectively. This is expected since the water flux is directly proportional to the water permeability coefficient as can be seen from Equation 2. A look at Equation 2 may lead to the erroneous conclusion that the relationship between A and J_w is linear. However, Figure 14 illustrates the non-linear effect that the change in A has on the water flux. On the other hand, an increase in the salt permeability coefficient results in a decrease in the water flux. This agrees with the inverse relationship between B and J_w that is demonstrated in Equation 2.

Flat-Sheet vs. Spiral-Wound Membranes

The coupon-scale run specifications for Run #1 in Table 2 were used as inputs to the PRO simulator in order to carry out a comparison between the power density and water flux values obtained using both the spiral-wound and flat-sheet membranes. In order to solely study the effect of changing the type of membrane unit on the power density and water flux, all the input conditions were kept the same for both the spiral-wound and flat-sheet units. The flat-sheet and spiral-wound membrane areas were both discretized into four elements each and the pumps and turbines were assumed to be 100% efficient. The flat-sheet run was carried out using co-current and counter-current flow of the draw and feed solutions. The assumption of perfect mixing on both sides of the membrane unit was used for both the spiral-wound and flat-sheet membrane units. As shown in Figure 15, the use of the spiral-wound membrane yields higher values of the water flux and power density than the flat-sheet membrane with co-current flow of the draw and feed solutions.

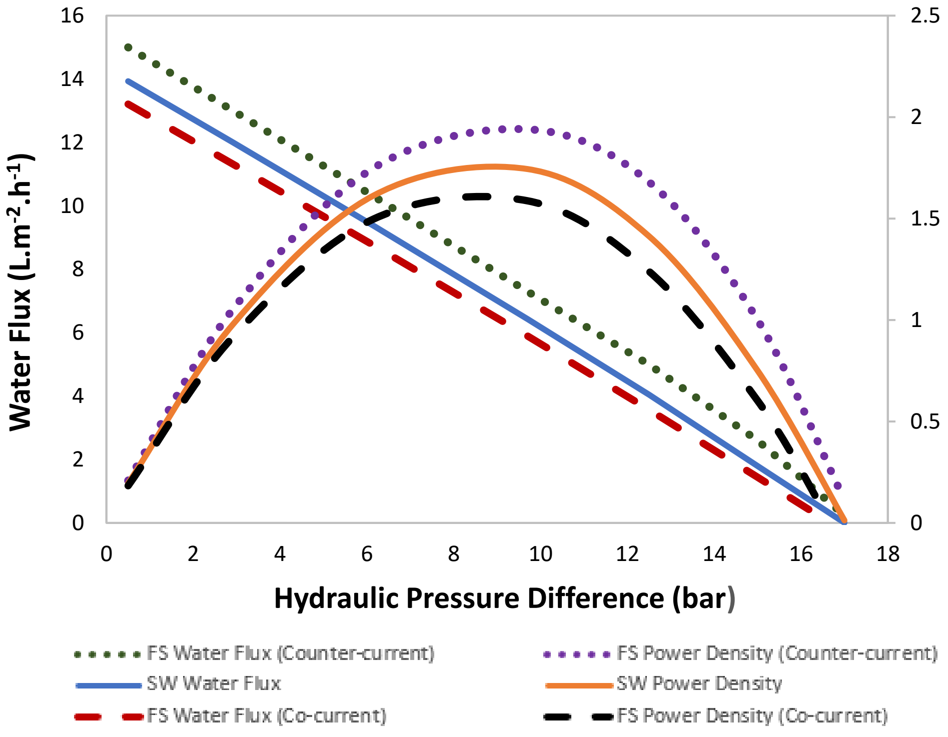

Figure 15: Comparison of power density and water flux for flat-sheet and spiral-wound membranes with 0.5 M NaCl draw solution and deionized water used as feed. HTI membrane characterization parameters were taken from Kim et al. [38]

As the hydraulic pressure difference increases, the difference in power density values is more pronounced. Similar trends, not shown in Figure 15, were observed for a draw solution concentration of 1 M NaCl. The differences in the power density and water flux values can be attributed to the cross-flow that occurs between the feed and the draw solutions of the spiral-wound membrane as can be seen in Figure 5. This cross-flow between the feed and draw solutions results in a more efficient mass transfer, which explains the higher water flux values that were obtained for the spiral-wound membrane case in comparison to the co-current flat-sheet membrane set up. The counter-current flow of the feed and draw solutions with the flat-sheet membrane yielded higher water flux and power density values than the spiral-wound membrane. This is expected since the counter-current flow of the feed and draw solutions optimizes the driving force of osmotic pressure difference and thus mass transfer, which increases the water flux values and power density.

The process simulator can also be used to run streams with more pronounced salinity differences, such as produced water and seawater due to the capability of the thermodynamic model to accurately predict thermodynamic properties over wide range of salt concentrations. We now consider a case in which the concentrations of the draw and feed solutions were 2.74 M and 0.6 M NaCl, respectively, with the produced water as the draw solution and the seawater as the feed solution. The remaining specifications were kept the same as those for Run #1 in Table 2. As in the previous coupon-scale run, the spiral-wound and flat-sheet membrane areas were discretized into four elements each and the pumps and turbines were assumed to be 100% efficient. The flat-sheet run was carried out using co-current and counter-current flow of the draw and feed solutions. The assumption of perfect mixing on both sides of the membrane unit was used for both the spiral-wound and flat-sheet membrane runs.

Figure 16 presents predictions of the water flux and power density values for this case.

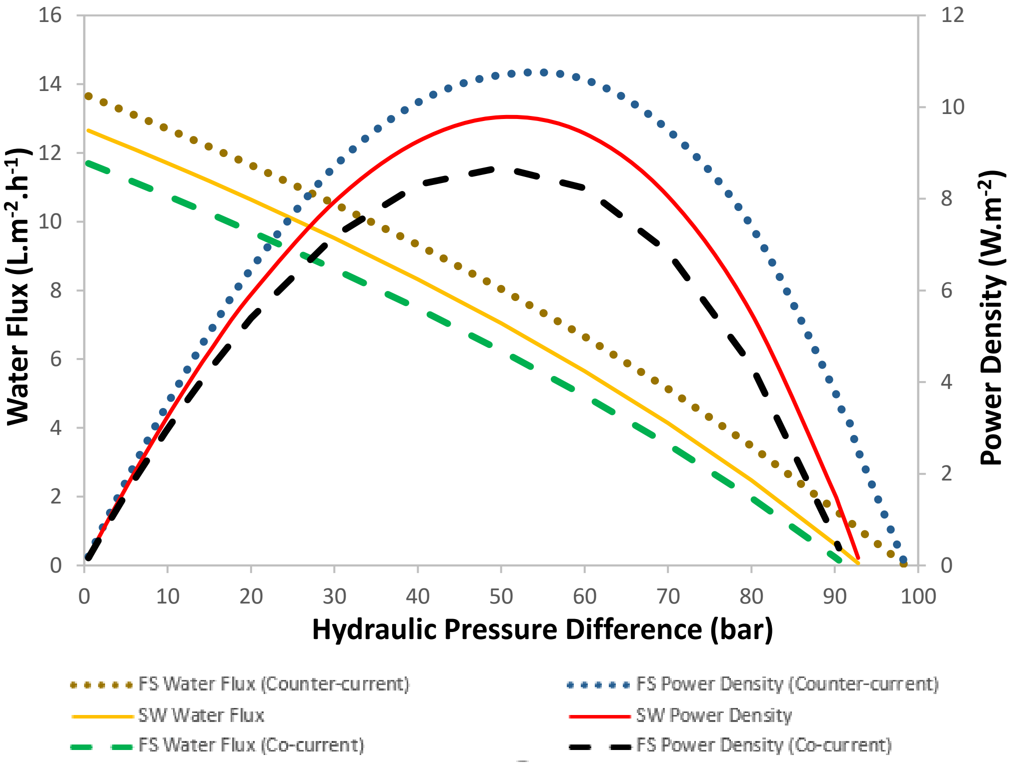

Figure 16: Comparison of power density and water flux for flat-sheet and spiral-wound membranes with 2.74 M NaCl draw solution and seawater (0.6 M NaCl) used as feed. HTI membrane characterization parameters were taken from Kim et al. [38]

The optimum values of power density obtained using a spiral-wound, flat-sheet membrane with co-current flow and flat-sheet membrane with counter-current flow were 9.8 W.m^{-2}, 8.7 W.m^{-2} and 10.7 W.m^{-2} respectively. The optimum power densities were obtained at a hydraulic pressure difference of about 50 bar. This is an interesting result because if the water flux is calculated with Equation 1, with the osmotic pressure difference predicted by the van't Hoff equation [40], it can be demonstrated that the maximum power density is obtained when the hydraulic pressure difference is equal to half of the osmotic pressure difference. In the case presented in Figure 16, this means that the optimum power density would occur at a hydraulic pressure difference of 46.5 bar. Nonetheless, with the use of a more accurate model for the diffusive mass transfer (Equation 2) and of a more accurate procedure for calculating the osmotic pressure difference, based on the Q-electrolattice EOS, it is obtained that the hydraulic pressure difference for maximum power density is higher – about 50 bar. The water flux and power density values obtained using the spiral-wound membrane were higher than those for the flat-sheet membrane with co-current flow at all hydraulic pressure differences. As explained in the previous example, the differences in the power density and water flux values are due to the cross-flow that occurs between the feed and the draw solutions in Zones I and III of the spiral-wound membrane. A more efficient mixing between the draw and feed solutions occurs due to the cross-flow in Zones I and III, this results in a larger water flux and thus power density than the co-current flow case with the flat-sheet membrane. The counter-current flow of the feed and draw solutions with the flat-sheet membrane was the optimum case and it yielded the highest values of water flux and power density. This is expected since the counter-current flow of the feed and draw solutions allows for a more efficient mass transfer, which results in an increase in the water flux and thus power density.

Figure 16 also illustrates the non-linear effect of the hydraulic pressure difference on the water flux (as demonstrated by Equation 2). Figure 15 might give the erroneous impression that the water flux changes linearly with the hydraulic pressure difference since the water flux curvature becomes more apparent when running the PRO simulator with higher salinities.

Internal Concentration Profiles

As solving the spiral-wound membrane module requires the discretization of the mathematical model, it is possible to determine local properties within the membrane unit. The concentration profiles shown in Figures 17 and 18 were generated by using a membrane area of 30 m^2 that was discretized into 16 elements with a glue-line fraction of 0.5. The draw and feed volumetric flowrates were 8.33×10^{-5} and 1.7×10^{-4} $m^3.s^{-1}$ respectively. The remaining specifications used were kept the same as those for Run #1 in Table 2. A hydraulic pressure difference of 6 bars, which lies within the operating range for the membrane, was used to generate the results and the pumps and turbines were assumed to be 100% efficient.

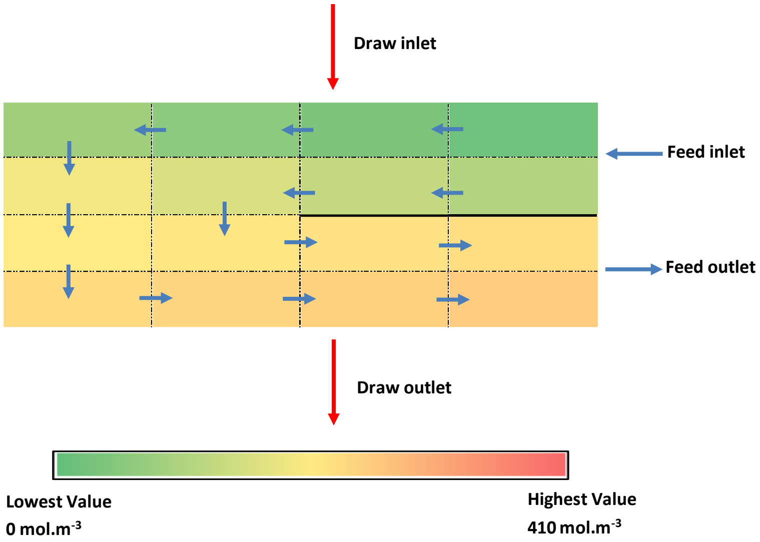

Figure 17: Internal NaCl feed concentration profile in a spiral-wound discretized membrane with 0.5 M NaCl draw solution and deionized water used as feed. HTI membrane characterization parameters were taken from Kim et al. [38]

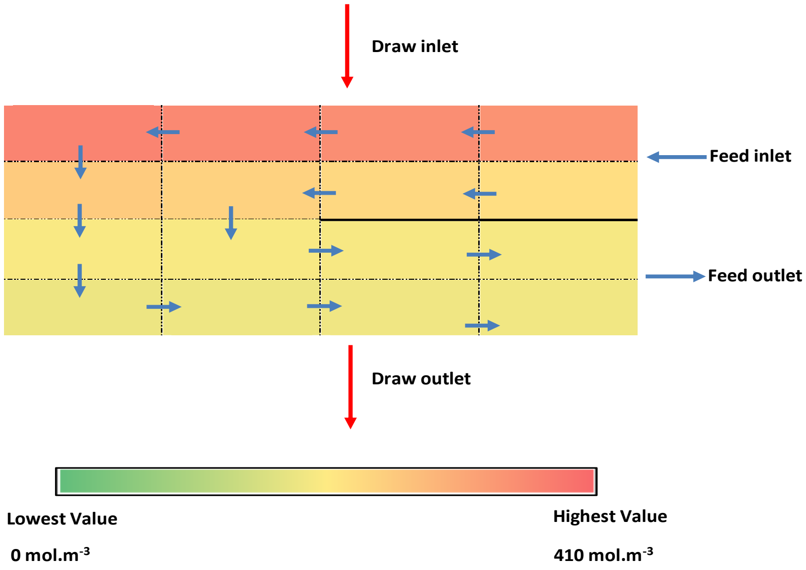

Figure 18: Internal NaCl draw concentration profile in a spiral-wound discretized membrane with 0.5 M NaCl draw solution and deionized water used as feed. HTI membrane characterization parameters were taken from Kim et al. [38]

The feed and draw flow patterns in the unwound spiral-wound membrane are illustrated in Figure 5. The feed solution flows through the membrane from Zone I to Zone II and Zone II to Zone III, whereas the draw solution flows across the membrane. As the feed solution flows within the spiral-wound membrane units, its NaCl concentration increases, as expected, since the solvent (water) ions will pass through the semi-permeable membrane from the feed solution into the draw solution. The discretized membrane model correctly predicts the expected trends, that is, the feed solution progressively increases in concentration following each subsequent element in the discretized membrane area and the draw solution decreases in concentration as it flows across the membrane unit. The lowest NaCl concentration is represented by the dark green color, whereas the highest NaCl concentration is represented by the dark pink color. For the NaCl feed concentration, the lowest value obtained was 5 mol.m^{-3} and the highest was 94 mol.m^{-3}. As for the NaCl draw concentration, the lowest value obtained was 312 mol.m^{-3} and the highest was 410 mol.m^{-3}.

Effect of the glue-line fractional length

An additional sensitivity analysis that was carried out using the process simulator aimed to study the effect of the glue-line fractional length on the power density. The input conditions that were used to obtain the power density values were kept the same as those in Table 3. The pumps and the turbines were assumed to be 100% efficient. The membrane area was discretized into 16 elements. The three cases that were compared are illustrated in Figure 19. The glue-line fractions that were used to make the comparison are 0.25, 0.5 and 0.75. The black nodes represent the points that belong to Zone I, the green nodes are in Zone II and the white nodes are in Zone III. The grey nodes represent the nodes that are on the glue-line (represented by the yellow line in Figure 19). The red arrows represent the draw inlet and the draw outlet, whereas the blue arrows represent the flow pattern of the feed solution which is impacted by the glue-line fraction. The results showed that as the glue-line fraction increased, the power density obtained decreased. The highest power density of 50.1 $W.m^{-2}$ was obtained when the glue-line fraction was set to 0.25. Power densities of 47.7 $W.m^{-2}$ and 44.9 $W.m^{-2}$ were obtained when the glue-line fraction was set to 0.5 and 0.75 respectively. The power density dropped by 10% when the glue-line fraction changed from 0.25 to 0.75, since an increase in the glue-line fraction impacted the feed flow pattern which resulted in a decrease in the overall performance. These power densities for Cases 1-3 were obtained for the cross-flow patterns of the feed and draw solutions in Zones I and III and co-current flow in Zone II as illustrated in Figure 19.

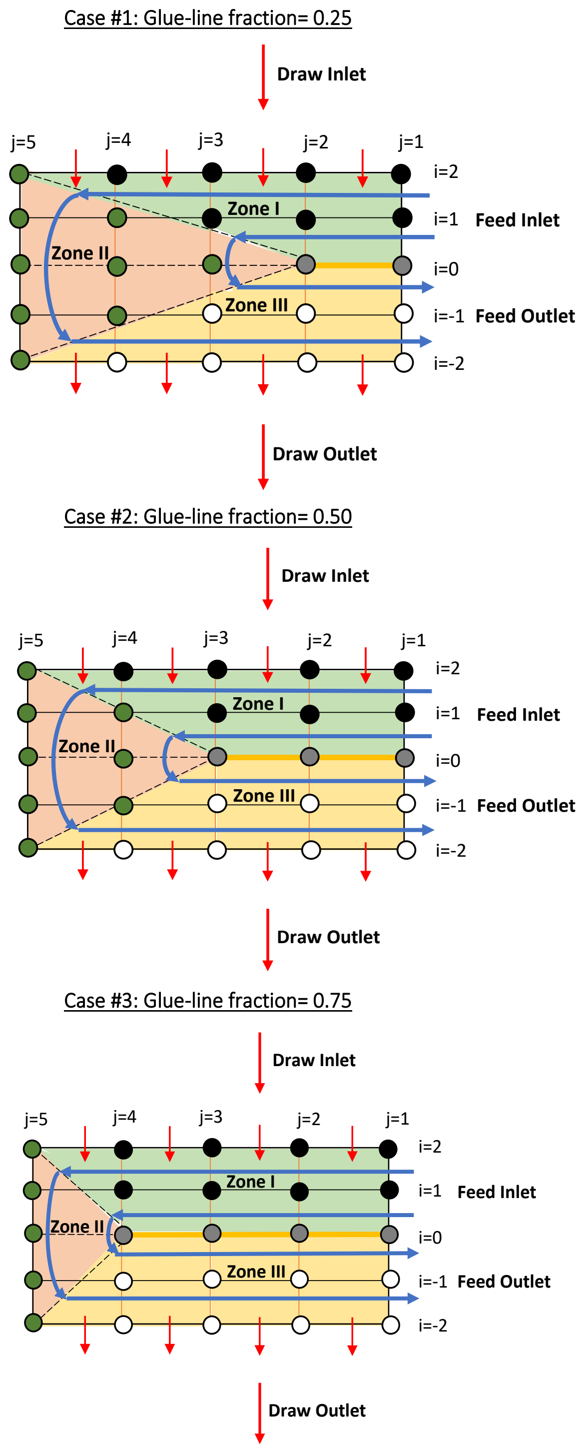

Figure 19: Comparison of cases with different glue-line fractions for a 4.1 M NaCl draw solution and seawater (0.6 M NaCl).

CHAPTER V

CONCLUSIONS

In this research work, a full-scale high salinity PRO process simulator was developed to model and analyze the performance of spiral-wound membranes taking into account dilution effects. The sensitivity analysis carried out showed that 4 discrete elements were deemed sufficient for the examples of this work but the formulation is flexible and can be used with more discrete elements for higher numerical accuracy. In order to obtain higher numerical accuracy for industrial size spiral wound modules, 16 elements were deemed sufficient for this work, as the results obtained from the PRO simulator closely matched those published in literature. The results obtained from the PRO simulator for this work were validated through comparison with published experimental data. Slight deviations between the simulator results and the published experimental results were observed at high hydraulic pressures. This was attributed to the effect of membrane deformation at high hydraulic pressure differences. The cases studied in this work showed that the use of a spiral-wound membrane yields higher values of power density than that of a flat-sheet membrane with co-current flow of the feed and draw solutions and lower values of power density than that of a flat-sheet membrane with counter-current flow. The examples studied showed that as the glue-line fraction increased, the power density obtained decreased. These results should provide guidelines for the conceptual design of pilot plants for additional developments and tests of this type of technology.

REFERENCES

[1] A. Achilli, T.Y. Cath, A.E. Childress, Power generation with pressure retarded osmosis: An experimental and theoretical investigation, Journal of Membrane Science, 343 (2009) 42-52.

[2] S. Loeb, Energy production at the Dead Sea by pressure-retarded osmosis: challenge or chimera?, Desalination, 120 (1998) 247-262.

[3] S. Loeb, One hundred and thirty benign and renewable megawatts from Great Salt Lake? The possibilities of hydroelectric power by pressure-retarded osmosis, Desalination, 141 (2001) 85-91.

[4] Q. She, X. Jin, C.Y. Tang, Osmotic power production from salinity gradient resource by pressure retarded osmosis: Effects of operating conditions and reverse solute diffusion, Journal of Membrane Science, 401 (2012) 262-273.

[5] S.E. Skilhagen, J.E. Dugstad, R.J. Aaberg, Osmotic power — power production based on the osmotic pressure difference between waters with varying salt gradients, Desalination, 220 (2008) 476-482.

[6] R.R. Gonzales, A. Abdel-Wahab, S. Adham, D.S. Han, S. Phuntsho, W. Suwaileh, N. Hilal, H.K. Shon, Salinity gradient energy generation by pressure retarded osmosis: A review, Desalination, 500 (2021) 114841.

[7] Y.C. Kim, Y. Kim, D. Oh, K.H. Lee, Experimental Investigation of a Spiral-Wound Pressure-Retarded Osmosis Membrane Module for Osmotic Power Generation, Environmental Science & Technology, 47 (2013) 2966-2973.

[8] R. Kaplan, D. Mamrosh, H.H. Salih, S.A. Dastgheib, Assessment of desalination technologies for treatment of a highly saline brine from a potential CO2 storage site, Desalination, 404 (2017) 87-101.

[9] A. Janson, D. Dardor, M. Al Maas, J. Minier-Matar, A. Abdel-Wahab, S. Adham, Pressure-retarded osmosis for enhanced oil recovery, Desalination, 491 (2020) 114568.

[10] J. Kim, K. Jeong, M.J. Park, H.K. Shon, J.H. Kim, Recent Advances in Osmotic Energy Generation via Pressure-Retarded Osmosis (PRO): A Review, Energies, 8 (2015) 11821-11845.

[11] D. Attarde, M. Jain, S.K. Gupta, Modeling of a forward osmosis and a pressure-retarded osmosis spiral wound module using the Spiegler-Kedem model and experimental validation, Separation and Purification Technology, 164 (2016) 182-197.

[12] A.P. Straub, S. Lin, M. Elimelech, Module-Scale Analysis of Pressure Retarded Osmosis: Performance Limitations and Implications for Full-Scale Operation, Environmental Science & Technology, 48 (2014) 12435-12444.

[13] N.Y. Yip, A. Tiraferri, W.A. Phillip, J.D. Schiffman, L.A. Hoover, Y.C. Kim, M. Elimelech, Thin-Film Composite Pressure Retarded Osmosis Membranes for Sustainable Power Generation from Salinity Gradients, Environmental Science & Technology, 45 (2011) 4360-4369.

[14] C.H. Tan, H.Y. Ng, Modified models to predict flux behavior in forward osmosis in consideration of external and internal concentration polarizations, Journal of Membrane Science, 324 (2008) 209-219.

[15] S. Zhao, L. Zou, Relating solution physicochemical properties to internal concentration polarization in forward osmosis, Journal of Membrane Science, 379 (2011) 459-467.

[16] J.R. McCutcheon, M. Elimelech, Influence of concentrative and dilutive internal concentration polarization on flux behavior in forward osmosis, Journal of Membrane Science, 284 (2006) 237-247.

[17] P. Nicoll, Forward Osmosis - A brief introduction, 2013.

[18] K.L. Lee, R.W. Baker, H.K. Lonsdale, Membranes for power generation by pressure-retarded osmosis, Journal of Membrane Science, 8 (1981) 141-171.

[19] P.J. Hickey, C.H. Gooding, Modeling spiral wound membrane modules for the pervaporative removal of volatile organic compounds from water, Journal of Membrane Science, 88 (1994) 47-68.

[20] A. Bhinder, S. Shabani, M. Sadrzadeh, Effect of Internal and External Concentration Polarizations on the Performance of Forward Osmosis Process, in: Osmotically Driven Membrane Processes-Approach, Development and Current Status., IntechOpen Limited London, UK, 2018, pp. 67-85.

[21] A.P. Straub, A. Deshmukh, M. Elimelech, Pressure-retarded osmosis for power generation from salinity gradients: is it viable?, Energy & Environmental Science, 9 (2016) 31-48.

[22] A. Achilli, J.L. Prante, N.T. Hancock, E.B. Maxwell, A.E. Childress, Experimental Results from RO-PRO: A Next Generation System for Low-Energy Desalination, Environmental Science & Technology, 48 (2014) 6437-6443.

[23] G. O'Toole, L. Jones, C. Coutinho, C. Hayes, M. Napoles, A. Achilli, River-to-sea pressure retarded osmosis: Resource utilization in a full-scale facility, Desalination, 389 (2016) 39-51.

[24] H. Manzoor, M.A. Selam, F.B. Abdur Rahman, S. Adham, M. Castier, A. Abdel-Wahab, A tool for assessing the scalability of pressure-retarded osmosis (PRO) membranes, Renewable Energy, 149 (2020) 987-999.

[25] H. Manzoor, M.A. Selam, S. Adham, H.K. Shon, M. Castier, A. Abdel-Wahab, Energy recovery modeling of pressure-retarded osmosis systems with membrane modules compatible with high salinity draw streams, Desalination, 493 (2020) 114624.

[26] F.-B.-A. Rahman, Modeling of Pressure Retarded Osmosis Using the Q-Electrolattice Equation of State, in: Chemical Engineering, Texas A&M University, 2017.

[27] N.Y. Yip, M. Elimelech, Thermodynamic and Energy Efficiency Analysis of Power Generation from Natural Salinity Gradients by Pressure Retarded Osmosis, Environmental Science & Technology, 46 (2012) 5230-5239.

[28] D. Attarde, M. Jain, K. Chaudhary, S.K. Gupta, Osmotically driven membrane processes by using a spiral wound module — Modeling, experimentation and numerical parameter estimation, Desalination, 361 (2015) 81-94.

[29] M.F. Naguib, J. Maisonneuve, C.B. Laflamme, P. Pillay, Modeling pressure-retarded osmotic power in commercial length membranes, Renewable Energy, 76 (2015) 619-627.

[30] J. Maisonneuve, P. Pillay, C.B. Laflamme, Pressure-retarded osmotic power system model considering non-ideal effects, Renewable Energy, 75 (2015) 416-424.

[31] C. Held, L.F. Cameretti, G. Sadowski, Modeling aqueous electrolyte solutions: Part 1. Fully dissociated electrolytes, Fluid Phase Equilibria, 270 (2008) 87-96.

[32] M.A. Selam, I.G. Economou, M. Castier, A thermodynamic model for strong aqueous electrolytes based on the eSAFT-VR Mie equation of state, Fluid Phase Equilibria, 464 (2018) 47-63.

[33] B. Maribo-Mogensen, K. Thomsen, G.M. Kontogeorgis, An electrolyte CPA equation of state for mixed solvent electrolytes, AIChE Journal, 61 (2015) 2933-2950.

[34] A. Zuber, R.F. Checoni, M. Castier, Thermodynamic properties of aqueous solutions of single and multiple salts using the Q-electrolattice equation of state, Fluid Phase Equilibria, 362 (2014) 268-280.

[35] A. Tamburini, F. Giacalone, A. Cipollina, F. Grisafi, G. Micale, Pressure retarded osmosis: A membrane process for environmental sustainability, Chemical Engineering Transactions, 47 (2016) 355-360.

[36] J.A. Myers, S.I. Sandler, R.H. Wood, An Equation of State for Electrolyte Solutions Covering Wide Ranges of Temperature, Pressure, and Composition, Industrial & Engineering Chemistry Research, 41 (2002) 3282-3297.

[37] A. Zuber, R.F. Checoni, R. Mathew, J.P.L. Santos, F. Tavares, M. Castier, Thermodynamic Properties of 1:1 Salt Aqueous Solutions with the Electrolattice Equation of State, Oil & Gas Science and Technology, 68 (2013) 255-270.

[38] Y.C. Kim, M. Elimelech, Adverse Impact of Feed Channel Spacers on the Performance of Pressure Retarded Osmosis, Environmental Science & Technology, 46 (2012) 4673-4681.

[39] Z.M. Binger, A. Achilli, Forward osmosis and pressure retarded osmosis process modeling for integration with seawater reverse osmosis desalination, Desalination, 491 (2020) 114583.

[40] J.H. Van't Hoff, The role of osmotic pressure in the analogy between solutions and gases, Journal of Membrane Science, 100 (1995) 39-44.

APPENDIX A

CALCULATION FLOWCHART

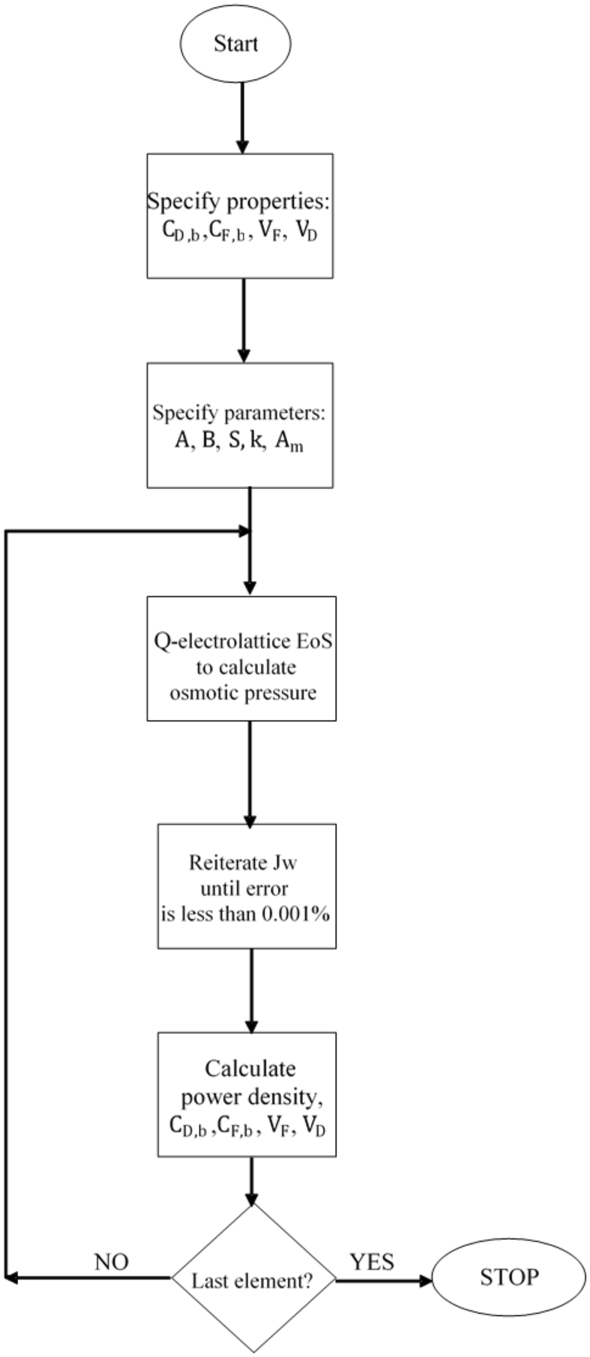

Figure 20: Calculation Procedure